DEVELOPMENT OF CARBON-FREE ZINC-AIR BATTERIES

A Thesis Submitted to
the Graduate School of Engineering and Sciences of
Izmir Institute of Technology
in Partial Fulfilment of the Requirements for the Degree of

MASTER OF SCIENCE

in Chemical Engineering

by

Yunus Emre BELET

March 2024
İZMİR

We approve the thesis of **Yunus Emre BELET**

Examining Committee Members:

Prof. Dr. Özgenç EBİL
Chemical Engineering, İzmir Institute of Technology

Assoc. Prof. Dr. Ayben TOP
Chemical Engineering, İzmir Institute of Technology

Asst. Prof. Dr. Halide DİKER
Solar Energy Institute, Ege University

5 March 2024

Prof. Dr. Özgenç EBİL
Supervisor, Chemical Engineering, İzmir Institute of Technology

Prof. Dr. Aysun SOFUOĞLU
Head of the Department of Chemical Engineering

Prof. Dr. Mehtap EANES
Dean of the Graduate School
of Engineering and Sciences

ACKNOWLEDGEMENTS

I want to thank all the people who contributed in some way to the work described in this thesis. First and foremost, I thank my advisor, Prof. Dr. Özgenç Ebil for accepting me into his research team. His advice and knowledge expanded my horizons in different topics throughout my thesis.

I also would like to thank Dr. Gizem Cihanoğlu. She conducted the AMAZE Project with me. I learned much from her. She was also a great teacher to me.

I also wanted to thank Prof. Dr. Muhsin Çiftçioğlu for the materials I used from his laboratory.

I want to thank all my friends in the Department of Chemical Engineering. I am thankful to my friends and lab mates Merve Karabıyık and Cansu Güler.

Finally, I wanted to thank my close friends and family, especially my mother, Adile Belet, and father, Lütfü Belet, for their support during the work. Their devotion to my academic career has made all these happen.

ABSTRACT

DEVELOPMENT OF CARBON-FREE ZINC-AIR BATTERIES

Zinc-air batteries are thought to be among the greatest substitutes for present energy storage systems because of their high energy densities (~1000 Wh/kg), affordability, and safety. However, zinc-air batteries face several problems, such as carbon corrosion, pore-clogging, and electrode passivation. The main cause of these problems is carbon in the air electrode. Therefore, carbon should be eliminated from the air electrode to enhance its performance. This thesis aims to synthesize an electrocatalyst for air electrodes for secondary carbon-free zinc-air batteries within the scope of the M-Era.NET "AMAZE" project.

Initially, manganese oxide was selected as an electrocatalyst and synthesized using a co-precipitation method with different parameters such as concentration, pH, temperature, and precursor materials. The best Mn_xO_y was obtained with a solution pH and temperature of 9.5 and 60°C, respectively. The main precursor for the catalyst was $KMnO_4$, with a ratio of $KMnO_4$:HCl as 20:4 by volume. α-MnO_2 with a surface area of 85.68 m^2g^{-1} was obtained. In addition, onset overpotentials for oxygen reduction and oxygen evolution reactions with 650mV and 271mV, respectively, and a maximum current density of 10.5 $mA.cm^{-2}$ were obtained. Nickel and cobalt additions were evaluated to improve ORR and OER activity. Catalyst with $Mn_xNi_yCo_zO_t$(1:0.5:0.5) composition performed better than other samples and had the highest surface area (172.06 m^2g^{-1}), ORR and OER potentials of 463mV and 700mV, respectively, and current density of 96 $mA.cm^{-2}$

ÖZET

KARBON İÇERMEYEN ÇİNKO-HAVA PİLLERİNİN GELİŞTİRİLMESİ

Çinko-hava bataryaları, sahip oldukları yüksek enerji yoğunluğu (~1000 Wh/kg), uygun maliyetleri ve güvenli olmaları nedeniyle günümüz enerji depolama sistemleri için en büyük ikameleri arasında olduğu düşünülmektedir. Ancak çinko-hava bataryalarının karbon korozyonu, gözenek tıkanması ve elektrot pasivasyonu gibi sorunlarla yüzleşmesi ve üstesinden gelmesi gerekmektedir. Bu bahsedilen problemlerin temelinde hava elektrodunda bulunan karbon bulunmaktadır. Bu sebeple hava elektrodundaki karbonun elimine edilmesi elektrodun performansını artıracaktır. Bu tez M-Era.NET "AMAZE" projesi kapsamında ikincil çinko-hava bataryaları için hava elektrodu geliştirmek ve bu elektrotta kullanılmak üzere elektrokatalizör sentezlemeyi amaçlamaktadır.

Elektrokatalizör olarak öncelikle manganez oksit seçilmiş ve konsantrasyon, pH, sıcaklık, öncül gibi farklı parametrelerle birlikte çöktürme yöntemi kullanılarak sentezlenmiştir. En iyi Mn_xO_y çözelti pH'ı ve sıcaklığı 9.5 ve 60°C koşullarında elde edilmiştir. Katalizör sentezi için kullanılan ana öncü malzeme $KMnO_4$ olarak belirlenmiştir ve bununla birlikte kullanılan HCl çözeltisi ile oranı hacimce 20:4($KMnO_4$:HCl) olacak şekilde ayarlanmıştır. Yapılan sentezler sonucu yüzey alanı 85.68 m^2g^{-1} α-MnO_2 elde edilmiştir. Ek olarak elde edilen katalizör oksijen indirgenme ve oksijen yükseltgenme reaksiyonları için sırasıyla 650mV ve 271mV potansiyelleri ve maksimum akım yoğunluğu olarak 10.5 $mA.cm^{-2}$ değeri göstermiştir. ORR ve OER aktivitelerini yükseltmek amacıyla nikel ve kobalt eklemesinde karar kılınmıştır. Bu eklemeler sonucunda üretilen $Mn_xNi_yCo_zO_t$(1:0.5:0.5) katalizör diğer katalizörlerden daha iyi sonuçlara ulaşmıştır. 172.06 m^2g^{-1}'lık yüzey alanıyla en yüksek yüzey alanı değerine ulaşan bu katalizör ORR ve OER için 463mV ve 700mV potansiyel değerleri ile 96 $mA.cm^{-2}$'lik bir akım yoğunluğuna ulaşmıştır.

TABLE OF CONTENTS

LIST OF FIGURES viii

LIST OF TABLES x

CHAPTER 1 INTRODUCTION 1

1.1. Batteries 2

1.1.1. Metal – Air Batteries 3

1.1.1.1. Zinc – Air Batteries 4

1.2. Motivation 4

1.3. Thesis Overview 5

CHAPTER 2 LITERATURE SURVEY 6

2.1. Metal – Air Batteries 6

2.1.1. Zinc – Air Batteries 8

2.1.1.1. Zinc Anode 11

2.1.1.2. Electrolyte 13

2.1.1.3. Gas Diffusion Eletrode (GDE) 14

CHAPTER 3 MOTIVATION 22

3.1. Carbon-free Catalyst Layer 22

3.2. Bifunctional Catalyst 23

3.3. Gas Diffusion Layer 24

3.4. AMAZE Project 24

CHAPTER 4 EXPERIMENTAL 25

4.1. Materials 25

4.2. Methods 25

4.2.1. Mn_xO_y Synthesis at Different pH Values 25
4.2.2. Mn_xO_y Synthesis at Different Temperatures 26
4.2.3. Mn_xO_y Synthesis with Different Precursors 26
4.2.4. $Mn_xNi_yCo_zO_t$ Synthesis 26
4.2.5. Physical and Morphological Characterization 27
4.2.6. Electrode Preparation 27
4.2.7. Electrochemical Characterization 28
4.3. Experimental Matrix 28
4.4. Synthesis Method Visual 29

CHAPTER 5 RESULST AND DISCUSSION 31
5.1. Effect of HCl Amount 31
5.2. Effect of pH 34
5.3. Effect of Temperature 37
5.4. Effect of Precursor and Precursor Concentration 48

CHAPTER 6 CONCLUSION 63

REFERENCES 65

APPENDIX A ELECTROCHEMICAL ANALYSIS RESULTS 75

LIST OF FIGURES

Figure **Page**

Figure 1.1. Global primary energy consumption by source (Ritchie, 2020) 1
Figure 2.1. Diagram of the working principle of a typical aqueous metal-air battery..... 7
Figure 2.2.Theoretical Energy Densities of several types of metal-air batteries (Li, 2017) 7
Figure 2.3. Schematic representation of Metal–Air Battery (Cadu, 2018) 9
Figure 2.4. Dendrite formation in anode (Garcia, 2017) 12
Figure 2.5. Schematic representation of Gas diffusion electrode (Kubannek, 2019) 15
Figure 4.1. Synthesis Method 30
Figure 5.1. SEM images of (a) (K)Mn_xO_y-20:2 and (b) (K)Mn_xO_y-20:4 32
Figure 5.2. XRD spectra of (K)Mn_xO_y-20:2 and (K)Mn_xO_y-20:4 samples 33
Figure 5.3.SEM images of (a) (K)Mn_xO_y-pH2, (b) (K)Mn_xO_y-pH7, (c) (K)Mn_xO_y-pH9.5@20°C and (d) (K)MnO_2-pH12..... 35
Figure 5.4.XRD spectra of (K)Mn_xO_y-pH2, (K)Mn_xO_y-pH7, (K)Mn_xO_y-pH9.5@20°C and (K)Mn_xO_y-pH12..... 36
Figure 5.5.SEM images of (a) (S)Mn_xO_y-pH9.5@20°C, (b) (S)Mn_xO_y-pH9.5@45°C and (c) (S)Mn_xO_y-pH9.5@60°C 38
Figure 5.6.XRD spectra of (S)Mn_xO_y-pH9.5@20°C, (S)Mn_xO_y-pH9.5@45°C and (S)Mn_xO_y-pH9.5@60°C 39
Figure 5.7. SEM images of (a) (K)Mn_xO_y-pH9.5@20°C, (b) (K)Mn_xO_y-pH9.5@45°C and (c) (K)Mn_xO_y-pH9.5@60°C 41
Figure 5.8. XRD spectra of (K)Mn_xO_y-pH9.5@20°C, (K)Mn_xO_y-pH9.5@45°C and (K)Mn_xO_y-pH9.5@60°C..... 42
Figure 5.9. Linear sweep voltammograms of (K)Mn_xO_y-20:2, (K)Mn_xO_y-pH9.5@60°C and (S)Mn_xO_y-pH9.5@60°C samples for (a) ORR and (b) OER 44
Figure 5.10.Cyclic voltammograms of (K)Mn_xO_y-20:2, (K)Mn_xO_y-pH9.5@60°C and (S)Mn_xO_y-pH9.5@60°C samples..... 46
Figure 5.11.Tafel plots of (K)Mn_xO_y-20:2, (K)Mn_xO_y-pH9.5@60°C and (S)Mn_xO_y pH9.5@60°C catalysts on nickel mesh for (a) OER and (b) ORR 47

Figure 5.12.SEM images of (S)$Mn_xNi_yCo_zO_t$(1:0.5:0.5)-pH9.5@60°C (a) 10 000x, (b) 50 000x and (S)$Mn_xNi_yCo_zO_t$(1:1:1)-pH9.5@60°C (c) 10 000x, (d) 50 000x. 49
Figure 5.13.SEM images of (K)$Mn_xNi_yCo_zO_t$(1:0.5:0.5)-pH9.5@60°C (a) 10 000x, (b) 50 000x and (K)$Mn_xNi_yCo_zO_t$(1:1:1)-pH9.5@60°C (c) 10 000x, (d) 50 000x 50
Figure 5.14. XRD graph of (S)$Mn_xNi_yCo_zO_t$(1:0.5:0.5)-pH9.5@60°C sample 52
Figure 5.15. XRD graph of (S)$Mn_xNi_yCo_zO_t$(1:1:1)-pH9.5@60°C sample 53
Figure 5.16. XRD graph of (K)$Mn_xNi_yCo_zO_t$(1:0.5:0.5)-pH9.5@60°C sample 54
Figure 5.17. XRD graph of (K)$Mn_xNi_yCo_zO_t$(1:1:1)-pH9.5@60°C sample 55
Figure 5.18.Linear Sweep Voltammogram of (K)Mn_xO_y-pH9.5@60°C, (K)$Mn_xNi_yCo_zO_t$(1:0.5:0.5)-pH9.5@60°C and (K)$Mn_xNi_yCo_zO_t$(1:1:1 pH9.5@60°C..... 57
Figure 5.19.Cycling Voltammogram of (K)Mn_xO_y-pH9.5@60°C, (K)$Mn_xNi_yCo_zO_t$(1:0.5:0.5)-pH9.5@60°C and (K)$Mn_xNi_yCo_zO_t$(1:1:1 pH9.5@60..... 59
Figure 5.20.Tafel Plot of (K)Mn_xO_y-pH9.5@60°C, (K)$Mn_xNi_yCo_zO_t$(1:0.5:0.5 pH9.5@60°C and (K)$Mn_xNi_yCo_zO_t$(1:1:1)-pH9.5@60°C for (a) ORR and (b) OER..... 60
Figure 5.21.Charge-Discharge Curves of (K)Mn_xO_y-pH9.5@60°C, (K)$Mn_xNi_yCo_zO_t$(1:0.5:0.5)-pH9.5@60°C and (K)$Mn_xNi_yCo_zO_t$(1:1:1 pH9.5@60°C..... 62

LIST OF TABLES

Table **Page**

Table 4.1. Experimental Matrix 29

Table 5.1. Chemical composition of samples regarding HCl amount as variable 33

Table 5.2. BET characterization results for (K)MnO_2-20:2, (K)MnO_2-20:4 34

Table 5.3. Chemical composition of samples regarding pH as a variable parameter 37

Table 5.4. BET characterization results for (K)MnO_2-pH2 and (K)MnO_2-pH12..... 37

Table 5.5. Chemical composition of samples regarding temperature as a variable parameter 40

Table 5.6. BET results for (S)Mn_xO_y-pH9.5@20°C, (S)Mn_xO_y-pH9.5@45°C and (S)Mn_xO_y-pH9.5@60°C samples 40

Table 5.7. Chemical composition of samples regarding temperature as a variable parameter 42

Table 5.8. BET characterization results for (K)Mn_xO_y-pH9.5@20°C, (K)Mn_xO_y-pH9.5@45°C, and (K)Mn_xO_y-pH9.5@60°C samples. 43

Table 5.9. Onset Potentials of (K)Mn_xO_y-20:2, (K)Mn_xO_y-pH9.5@60°C and (S)Mn_xO_y-pH9.5@60°C samples for ORR 45

Table 5.10. Tafel slopes of catalysts on Ni-mesh for ORR and OER 48

Table 5.11. EDX results of (S)$Mn_xNi_yCo_zO_t$(1:0.5:0.5)-pH9.5@60°C sample..... 51

Table 5.12. EDX results of (K)$Mn_xNi_yCo_zO_t$(1:0.5:0.5)-pH9.5@60°C and (K)$Mn_xNi_yCo_zO_t$(1:1:1)-pH9.5@60°C sample..... 51

Table 5.13. Chemical composition of (S)$Mn_xNi_yCo_zO_t$(1:0.5:0.5)-pH9.5@60°C sample 52

Table 5.14. Chemical composition of (S)$Mn_xNi_yCo_zO_t$(1:1:1)-pH9.5@60°C sample . 53

Table 5.15. Chemical composition of (K)$Mn_xNi_yCo_zO_t$(1:0.5:0.5)-pH9.5@60°C sample 54

Table 5.16. Chemical composition of (K)$Mn_xNi_yCo_zO_t$(1:1:1)-pH9.5@60°C sample.. 55

Table 5.17. BET Analysis results of samples..... 56

Table 5.18. Onset Overpotential Values of (K)Mn_xO_y-pH9.5@60°C, (K)$Mn_xNi_yCo_zO_t$(1:0.5:0.5)-pH9.5@60°C and (K)$Mn_xNi_yCo_zO_t$(1:1:1)-pH9.5@60°C..... 58

Table 5.19. Tafel Slopes of Catalyst for ORR and OER..... 61

CHAPTER 1

INTRODUCTION

Due to the worldwide efforts to reduce greenhouse gas emissions and convert to a low-carbon economy, the demand for effective and sustainable energy storage technologies has been rising quickly in recent years (IEA, 2020). Therefore, alternative energy production methods have attracted interest gradually over the years. Figure 1.1 shows the global primary energy consumption by source. When we only look at 2019, the global energy consumption is calculated as 173,340 TWh (Ritchie, 2020). Although the use of renewable alternative energy sources has increased over the years, it is still insufficient. At this point, the world is facing an energy crisis due to its dependence on fossil fuels.

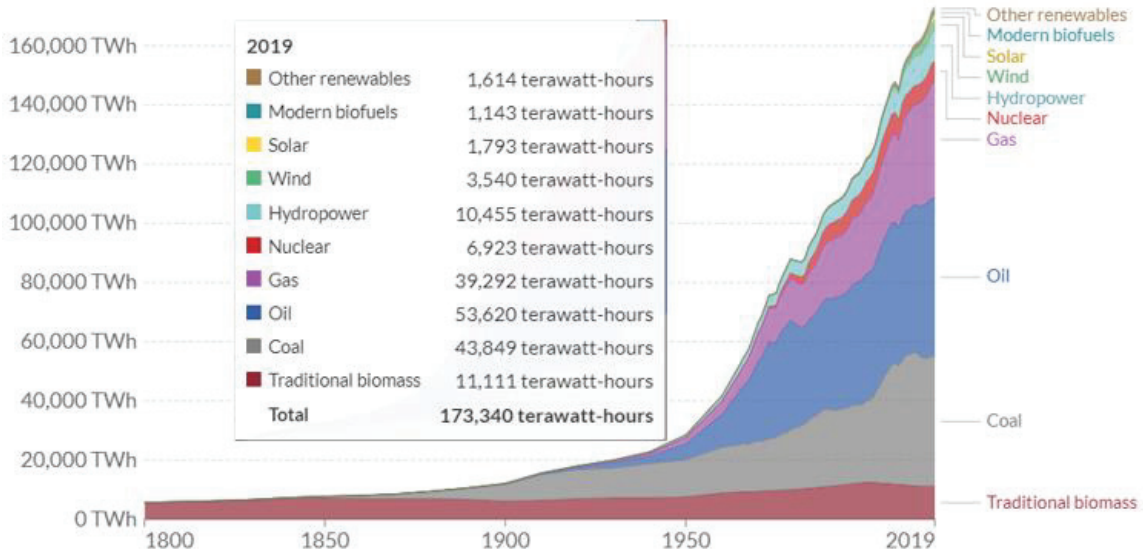

Figure 1.1. Global primary energy consumption by source (Ritchie, 2020)

Energy storage technologies are essential in integrating renewable energy sources into the current power grid, addressing intermittent issues, and providing a reliable and sustainable power supply (Chen et al., 2017). Batteries have become one of

the most promising energy storage sources and have gradually attracted interest over the energy density, scalability, and relatively low environmental impact (Lu et al., 2017).

1.1. Batteries

Batteries are the basic building block of electrochemical energy. A battery is a device that uses an electrochemical oxidation-reduction mechanism to convert chemical energy into electricity. Batteries are built in such a way that the energetically beneficial redox reaction may occur when electrons flow through the circuit's exterior parts.

Batteries are divided into two groups as non-rechargeable (primary) and rechargeable (secondary). Primary batteries usually have high energy density and discharge slowly. Because there is no electrolyte inside these cells, they are often referred to as dry cells. The chemical reaction is irreversible, and the internal resistance is substantial. Its initial cost is low, and primary cells are simple to employ. Secondary batteries are composed of liquid salts and wet cells and have a low energy density. Internal resistance is low, and the chemical process can be reversed. When compared to the primary batteries, they usually have a higher initial cost and are more difficult to utilize (Crompton, 2000).

Lithium-ion batteries are extensively employed due to their high energy density (150 to 200 Wh/kg), lengthy cycle life, and low self-discharge rate. (Dunn, 2011). They use carbon-based materials as anodes and lithium compounds as cathodes. Low self-discharge rate, a long cycle life, and high energy density are all benefits of lithium-ion batteries. They do, however, have drawbacks, including a brief lifespan overall and safety issues brought on by their flammable and reactive nature (Scrosati, 2010).

On the other hand, metal-air batteries utilize oxygen from the air as the cathode reactant. They use metal anodes, such as zinc or lithium, and porous cathodes for oxygen diffusion. Due to the abundant availability of oxygen from the air, metal-air batteries have benefits, including higher theoretical energy densities and less weight (Liang, 2017). However, they have drawbacks, such as shorter cycle lifetimes and sensitivity to external variables like temperature and humidity (Liang, 2017).

1.1.1. Metal – Air Batteries

Metal–air batteries use design elements from both traditional batteries and fuel cells. The basic metal–air battery assembly includes a metal anode, an air-breathing cathode, and an electrolyte that fits for both electrodes to give better performance.

The working principle of metal-air batteries is based on the energy obtained from anode and cathode half-cell reactions. Equation (1.1), (1.2) (Li, 2017) shows anode and cathode reactions:

Anode:

$$M \leftrightarrow M^{n+} + ne^{-} \tag{1.1}$$

Cathode:

$$O_2 + ne^{-} \leftrightarrow 2H_2O + 4OH^{-} \tag{1.2}$$

There are many types of metal–air batteries and various classifications for them. However, they can be basically classified as aqueous and non-aqueous metal–air batteries according to their electrolytes.

The ionic conductivity of the aqueous electrolyte is quite high. Furthermore, aqueous electrolytes are appealing for high-power-density batteries. In addition, aqueous electrolytes are nonflammable and inexpensive (Olabi, 2021). Solid-state electrolytes offer the potential to reduce electrolyte leakage while preserving thermal stability and resilience. They also can minimize electrolyte evaporation and gas crossover issues (Olabi, 2021).

Metal–air batteries can also be classified according to their anode metal. The most common of them are zinc-air, aluminum-air, sodium-air, lithium-air, magnesium-air, iron-air, and Potassium-air batteries. Figure 1.2. shows theoretical energy densities of various metal-air batteries. Each type of metal-air battery has certain advantages and disadvantages. For example, Li-air batteries have higher theoretical energy density (10,000 Wh/kg), potentially surpassing other batteries. However, the problems in developing stable electrolytes and many side reactions prevent them from being suitable candidates for the energy storage technologies of the future. On the other hand, Al-air batteries have a high energy density (3,500 Wh/kg), but it is difficult to prevent corrosion due to the high activity of aluminum. When all metal-air batteries are compared, their high energy density, environmental friendliness, lightweight, cost of

materials and manufacturing, and scalability make Zn-air batteries one step ahead of metal-air batteries.

1.1.1.1. Zinc – Air Batteries

Zinc-air batteries have been around since the 19th century. One of the first batteries was Alessandro Volta's voltaic pile, which produced electricity in 1800 using copper and zinc electrodes and an electrolyte. Despite not being a real zinc-air battery, it helped establish the electrochemical characteristics of zinc (Kordesh, 1980). In the 1930s, the modern zinc-air battery as we know it today began to take shape. Researchers first tried using air or oxygen as the cathode to generate electrical energy (Whittingham, 1977). Research efforts in the 1980s and 1990s were concentrated on enhancing the performance and lifetime of zinc-air batteries. More effective electrolytes and materials for air electrodes have been developed (Aurbach, 2009). With numerous applications, zinc-air batteries have become a potential new energy storage technology. In the world of electric cars (EVs), attention has been drawn to their high energy density, which may provide longer driving ranges between charges (Liang, 2018). Zinc-air batteries also have a position in the world of portable electronics, especially in items like hearing aids where durable and dependable power sources are essential (Li, 2017).

1.2. Motivation

Essentially, the motivation of this study is to address the problems arising from the air electrode of zinc-air batteries, then reach a solution to these problems and take a step towards the commercialization of zinc-air batteries.

1.3. Thesis Overview

In Chapter 2, detailed specific information was presented about Zinc–air batteries and gas diffusion electrodes, their problems of them, and how to prevent the challenges.

In Chapter 3, the motivation for the work was described.

In Chapter 4, the experimental work of the research and characterization methods are explained in detail.

In Chapter 5, the results of the physical and electrochemical characterization and performance tests of produced air electrodes are investigated.

Chapter 6 includes the conclusion part of the thesis and discusses future aspects of the research.

CHAPTER 2

LITERATURE SURVEY

A detailed literature survey on gas diffusion electrodes of zinc–air batteries was investigated in this chapter. Advantages, bottlenecks, and how to solve these bottlenecks were examined in order to commercialize zinc–air batteries.

2.1. Metal – Air Batteries

Compared to Li-ion batteries, research on metal-air batteries was started far earlier. Maiche created the primary zinc-air battery in 1878, and its products were first made available for purchase in 1932. Later, in the 1960s, aqueous Mg-air, Al-air, and Fe-air batteries were created. About 20 years ago, non-aqueous metal-air batteries such as Li-air, Na-air, and K-air began to appear (Yaqoob, 2022). Research and development have placed a substantial emphasis on the zinc-air battery, and subsequently, better materials and designs allowed for its commercial usage in small electrical devices like hearing aids (Savadogo, 2014).

As the need for effective and sustainable energy storage systems grows, metal-air batteries have attracted a lot of interest in recent years. Metal-air batteries are a type of electrochemical energy storage device that produces electrical energy through the electrochemical reaction of a metal anode with oxygen from the air. Their potential high energy density (up to 10000 Wh/kg) makes them suited for a variety of applications. The working principle behind metal–air batteries is the oxidation of the metal anode and the oxygen reduction at the cathode, which can be referred to as the air electrode (Zhang, 2020). The working principle can be followed from the diagram in Figure 2.1 as well.

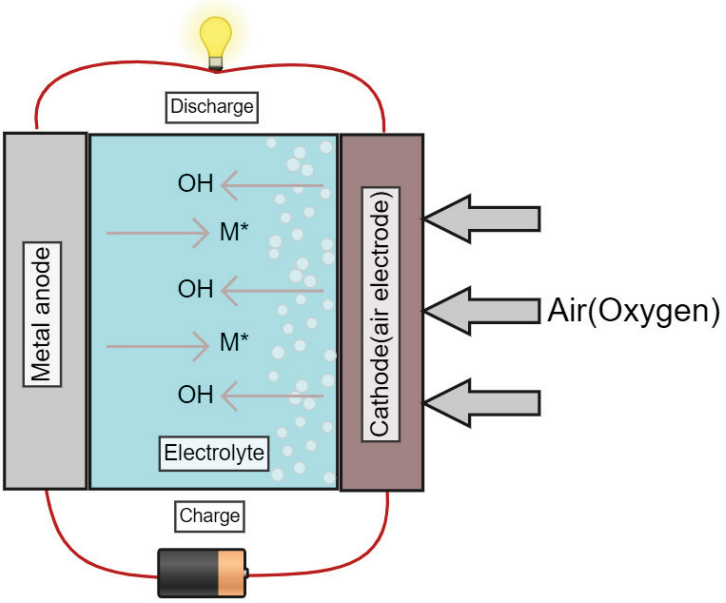

Figure 2.1. Diagram of the working principle of a typical aqueous metal-air battery

Metal-air batteries are classified according to the metal used in the anode, such as zinc, lithium, aluminum, iron, magnesium, sodium, and potassium (Li, 2017).

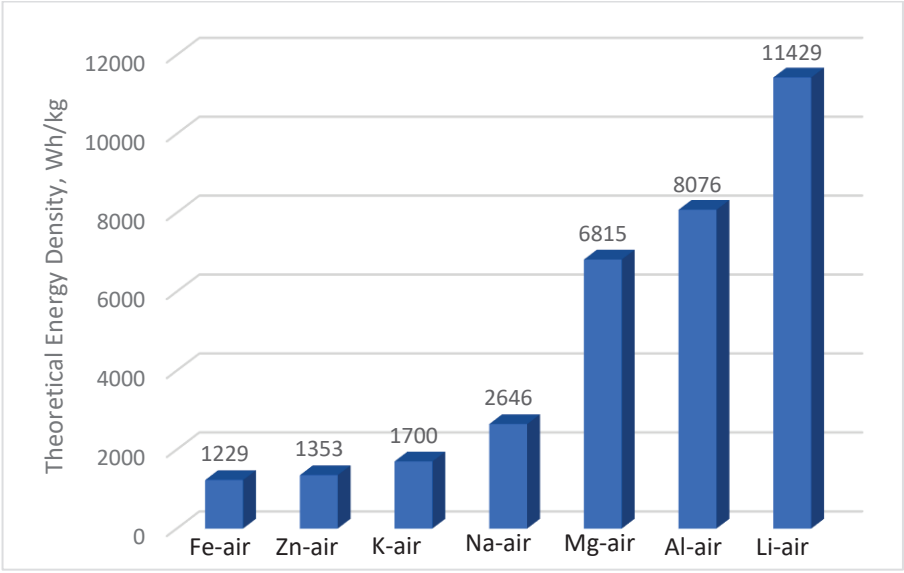

Figure 2.2. Theoretical Energy Densities of several types of metal-air batteries (Li, 2017)

Compared to other metal-air batteries, lithium-air stands out because its energy content (6000 kJ/kg) is almost as high as that of diesel fuel or almost 100 times that of current lithium-ion batteries (Torabi, 2020). This makes lithium–air batteries such an attractive solution for energy storage crises. However, they have several drawbacks: Due to problems including cathode corrosion and the buildup of reaction byproducts, lithium-air batteries frequently have a limited cycle life, which could affect their long-term durability (Bruce, 2012). Lithium–air batteries can generate reactive oxygen species during the discharge process, which can be dangerous if poorly handled. Thermal runaway, along with fire risks, may result from this (Lu, 2013). In lithium-air batteries, the electrolyte is highly reactive with the lithium anode, which causes the electrolyte to break down and solid electrolyte interphase (SEI) to grow on the lithium surface. The effectiveness and efficiency of the battery may be reduced (Cheng, 2017). In addition, due to the mining and manufacturing of lithium, which can have damaging ecological and social implications, the manufacture and recycling of lithium-air batteries might cause environmental concerns (Mudd, 2017).

On the other hand, zinc-air batteries have fewer reversibility issues compared to lithium-air batteries. Lithium peroxide production and breakdown during cycling in lithium-air batteries can lead to irreversible capacity loss (Chen, 2015), and zinc is more accessible and less expensive than lithium; manufacturing costs for zinc-air batteries may be reduced (Gonçalves, 2020). Also, zinc–air batteries have longer shelf lives compared to lithium-air batteries (Muzaffar, 2015). Due to the lower typical electrode potentials of sodium and potassium, sodium-air and potassium-air batteries may have an energy density that is comparable to or less than zinc-air batteries (Lee, 2015). Compared to several other metals used in metal-air batteries, zinc is considerably more eco-friendly and less harmful (Nazri, 1984).

2.1.1. Zinc – Air Batteries

Zinc-air batteries stand out as a very practical option among the many metal–air systems due to their high theoretical energy density (1086 Wh/kg), efficiency, safety, and environmentally friendly nature. Zinc-air batteries have a theoretical energy density

of 1086 Wh/kg, which is approximately five times greater than that of Li-ion batteries. In addition, their operating cost is thought to be less than $10/kWh, making them a much more cost-effective alternative to Li-ion batteries. The zinc-air battery system has been developed and has been successfully used in a wide range of products, including hearing aids, medical equipment, navigation devices, and railway signaling systems.

There are two varieties of zinc-air rechargeable batteries: mechanical and electrical rechargeable batteries. When using a mechanically rechargeable battery, the old zinc electrode is swapped out with a new one. This solved the issue of unstable, bifunctional air electrodes and the reversibility of bad zinc electrodes. However, this solution is limited by the high expense of the zinc supply stations and recharging network (Fu, 2016).

On the other hand, zinc-air batteries that can be electrically recharged have an exciting potential thanks to the bifunctional air electrodes. New bifunctional air electrodes and bifunctional oxygen electrocatalysts, which can support both the oxygen reduction reaction (ORR) during discharge and the oxygen evolution reaction (OER) during charging are introduced to achieve this rechargeability.

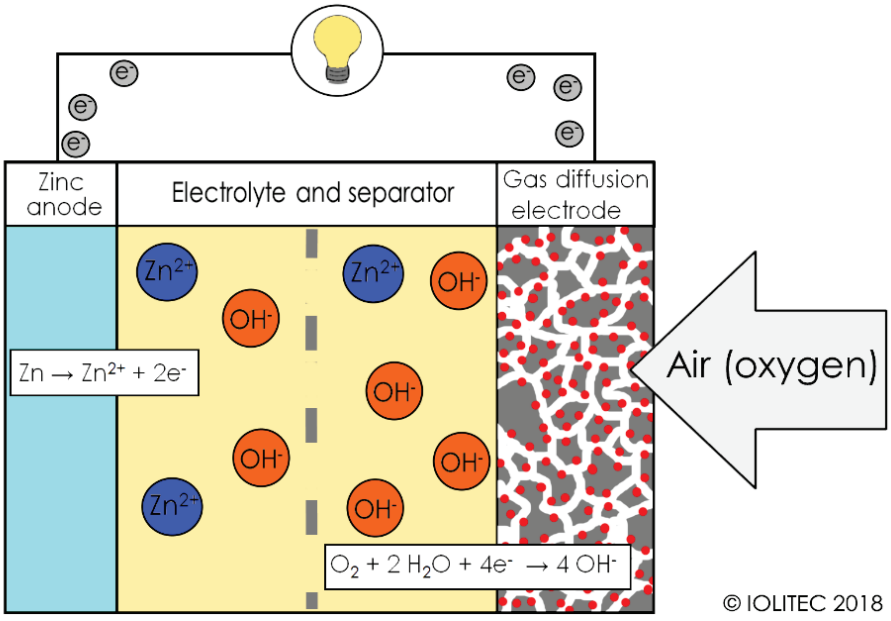

Figure 2.3. Schematic representation of Metal–Air Battery (Cadu, 2018)

A typical alkaline aqueous zinc–air battery structure is shown in Figure 2.3. Zinc–air batteries are made up of three main parts: the zinc anode, the cathode, also known as the air electrode (gas diffusion electrode, GDE), and the electrolyte. In a zinc-air battery, the anode is commonly constructed of zinc, which acts as the energy source. Zinc oxidizes during discharge, releasing electrons. During the reduction half-reaction, oxygen from the air combines with electrons and water at the cathode to form hydroxide ions. The electrolyte, frequently an alkaline solution, divides the anode and cathode. It enables ion movement between the two electrodes.

Equations (2.1) - (2.8) show the anode, cathode, and overall reactions (Lee, 2010) for Zinc–air batteries. The metallic zinc electrode is oxidized with OH^- during battery discharge, yielding soluble zincate ions. When these zincate ions get supersaturated in the medium, they decompose into insoluble zinc oxides. In the meantime, atmospheric oxygen gas diffuses into the cathode. ORR then occurs at the three-phase boundary between the air electrode, liquid electrolyte, and gas phase. The produced hydroxyl ions travel through the electrolyte from the air electrode to the metal anode, completing the process. These chemical pathways are reversible and occur when the battery is recharged.

Discharge

Anode:

$$Zn^{2+} + 4OH^- \rightarrow Zn(OH)_4^{2-} \quad (2.1)$$

$$Zn(OH)_4^{2-} \rightarrow ZnO + H_2O + 2OH^- \quad (2.2)$$

Cathode:

$$O_2 + 2H_2O + 4e^- \rightarrow 4OH^- \quad (2.3)$$

Overall:

$$2Zn + O_2 \rightarrow 2ZnO \quad (2.4)$$

Recharge

Anode:

$$ZnO + H_2O + 2OH^- \rightarrow Zn(OH)_4^{2-} \quad (2.5)$$

$$Zn(OH)_4^{2-} 2e^- \rightarrow Zn + 4OH^- \quad (2.6)$$

Cathode:

$$4OH^- \rightarrow O_2 + 2H_2O + 4e^- \quad (2.7)$$

Overall:

$$2ZnO \rightarrow 2Zn + O_2 \quad (2.8)$$

The theoretical operating voltage of zinc–air batteries is 1.65 V, according to the reaction process. However, to maintain a suitable discharge current density, their practical operating voltages during discharge are lower, often around 1.4 V. To reverse the reaction, a recharge voltage of around 2 V or higher is required. The significant overpotentials of the oxygen reaction at the air cathode are primarily responsible for such noticeable divergence from the equilibrium value (Jiao, 2014).

2.1.1.1. Zinc Anode

Metallic zinc has a long history of being a preferred anode material due to its favorable characteristics, which include a significant specific energy density, a constant discharge voltage, cost-effectiveness, and eco-friendliness. Although the anode in zinc-air batteries has traditionally been pure zinc metal, a tremendous amount of effort has been made to improve the zinc electrode. The surface properties of zinc are often critical in achieving a fast reaction rate in an alkaline electrolyte. It has also been explored that zinc electrode materials with increased surface areas, such as nanoparticles (Peng, 2023), nanowires (Ezeigwe, 2020), and foam (Li, 2013), show improved performance rather than bulk zinc anodes. These zinc structures with an increased surface area are used in applications requiring large discharge currents. However, the increased surface area causes a higher corrosion rate, which has negative effects on safety, battery longevity, and zinc consumption efficiency.

When considering a zinc anode, there are several drawbacks that need to be addressed and overcome. The growth of zinc dendrites while a battery is operating is one of the main problems with zinc anodes. On the anode's surface, dendrites, which resemble trees, develop as the battery is charged and discharged. The dendrite structures can be seen in Figure 2.4. These dendrites could lead to internal short circuits, which would shorten the life of the battery and be dangerous (Liang, 2017). Different methods can be used to prevent dendrite formation. Electrolyte modification and anode engineering can also be used. For example, adding metal ions such as Pb^{2+}(Wen, 2012), Bi^{3+}(Wang, 2001) and In^{3+}(Leung, 2011) to electrolyte solution can be used to prevent

dendrite formation. Also, the use of copper (Leung, 2011), nickel (Cheng, 2013), lead (Cheng, 2013), etc., in the anode can improve the characteristics of the anode against dendrite formation. In addition to that, dendrite formation can be prevented on the zinc electrode by applying surface treatments or coatings. A smoother electrode surface can be maintained with the use of materials like polymer coatings or conductive nanoparticles (Wang, 2023).

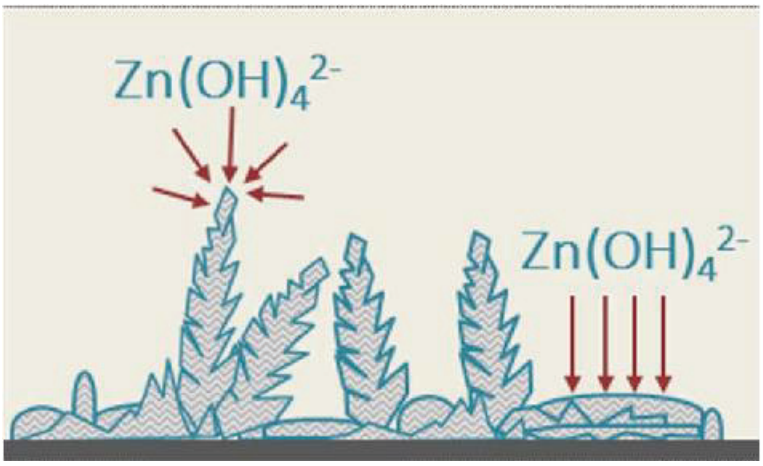

Figure 2.4. Dendrite formation in anode (Garcia, 2017)

Zinc from the anode dissolving into the electrolyte can cause capacity loss and reduced battery performance. Zinc ions can plate on the cathode when they dissolve into the electrolyte, resulting in passivation and a reduction in the overall efficiency of energy conversion (Wu, 2018). To prevent this, the electrolyte needs to be modified. For example, for KOH electrolyte systems, the molarity of the KOH solution should not exceed 6 M (Liu, 2018).

The operation and design of zinc-air batteries depend on the zinc's passivation. Passivation is the process of creating a thin, protective layer on the zinc electrode's surface to stop unintended side effects and improve the battery's overall performance. Due to the fact that zinc-air batteries rely on the controlled oxidation of zinc, this process is especially crucial. The process of creating a stable coating of zinc oxide on the surface of the zinc electrode is known as zinc passivation in zinc-air batteries. This layer serves as a barrier, preventing the zinc underneath from oxidizing further and guaranteeing that the necessary electrochemical reactions take place. The zinc electrode

is exposed to oxygen from the air, which triggers a series of chemical processes that result in the creation of this protective coating (Hosseini, 2018). The electrolyte can have specific additions to prevent passivation. For instance, it's investigated that the usage of organic compounds like bipyridine and amines can help zinc dissolve without being too oxidized, hence reducing the amount of ZnO that forms (Chen, 2020). In addition to that, the zinc surface can benefit from coatings or surface treatments to lessen passivation. For instance, it has been investigated that shields made of graphene, carbon nanotubes, and other polymers are used to shield zinc from electrolytes and avoid ZnO production (Tao, 2022).

Energy losses and a reduction in battery performance can result from side reactions at the anode. These unwanted electrochemical events, such as the production of gaseous hydrogen and hydrogen peroxide, can occur at the zinc anode. By diverting electrons from the desired electrochemical process, these side reactions reduce the amount of energy generated (Liang, 2017). The anode may corrode with time, reducing the amount of surface area that may be used for electrochemical reactions. The capacity of the battery and lifetime may be restricted by anode corrosion (Wu, 2018).

2.1.1.2. Electrolyte

There are two types of electrolytes: aqueous and non-aqueous. Aqueous electrolytes are divided into three groups: alkaline, neutral, and acidic. Non-aqueous electrolytes are divided into three groups: solid polymers, gel polymers, and room-temperature ionic liquid electrolytes (Mainar, 2018).

Zinc is thermodynamically unstable in aqueous solutions, as seen by the Pourbaix diagram of zinc, which depicts the reactions of zinc in aqueous solutions and conditions of equilibrium. Over the complete pH range, it begins to dissolve with the evolution of hydrogen. This graphic indicates that zinc has great solubility and dissolves with the generation of Zn^{2+} ions in acidic environments where no zinc surface oxides are stable. Even so, oxide coatings can form between pH 4 and 6, but they are porous and do not passivate. On the other hand, more stable zinc corrosion products ($Zn(OH)_2$)

are produced in neutral or slightly alkaline solutions because zinc solubility declines with rising pH in acidic solutions (Mainar, 2016).

The inherent electrochemical reversibility and quick electrochemical kinetics of zinc, along with the high ionic conductivity of the electrolyte, good low-temperature performance, and high solubility of zinc salts, have made an alkaline electrolyte battery with a zinc anode desirable (Shaigan, 2010).

The most common electrolytes in zinc-based batteries, such as Ni-Zn or Zn-Air, are alkaline aqueous solutions that comprise lithium hydroxide, sodium hydroxide, and potassium hydroxide. However, because of the zinc salts' great solubility and quick electrochemical kinetics, KOH has been utilized the most among them.

On the other hand, compared to an alkaline electrolyte, the neutral electrolyte has two main advantages: (i) it does not carbonize, and (ii) it minimizes dendrite growth. The secondary zinc-air batteries' cycle life may be extended for both reasons. These benefits result from the electrolyte's "neutral" pH, which lowers zinc solubility.

Because of their short life cycles and the need for an appropriate catalyst and support to overcome issues with the air electrode's catalytic activity, acid electrolytes have not been used extensively in rechargeable zinc-air batteries.

As non-aqueous electrolytes, organic electrolytes have the ability to counteract a variety of drawbacks, including dendrite development, water evaporation-induced electrolyte dry-out, hydrogen evolution, and alkaline electrolyte carbonation. They offer a somewhat wider electrochemical window and a greater temperature range.

However, it is crucial to choose the right composition to prevent the dangers of volatility, toxicity, and flammability in non-aqueous metal-air batteries.

2.1.1.3. Gas Diffusion Eletrode (GDE)

Gas diffusion electrodes consist of a porous catalyst layer that is placed onto a carrier material. The electron-conducting catalyst layer catalyzes a reaction between the liquid and gaseous phases. As a result, the gas, electrolyte, and catalyst must all be connected. This is known as the three-phase interface, where the solid, liquid, and

gaseous phases come into contact. Figure 2.5. shows the typical gas diffusion electrode setup (Hernandez-Aldave, 2020).

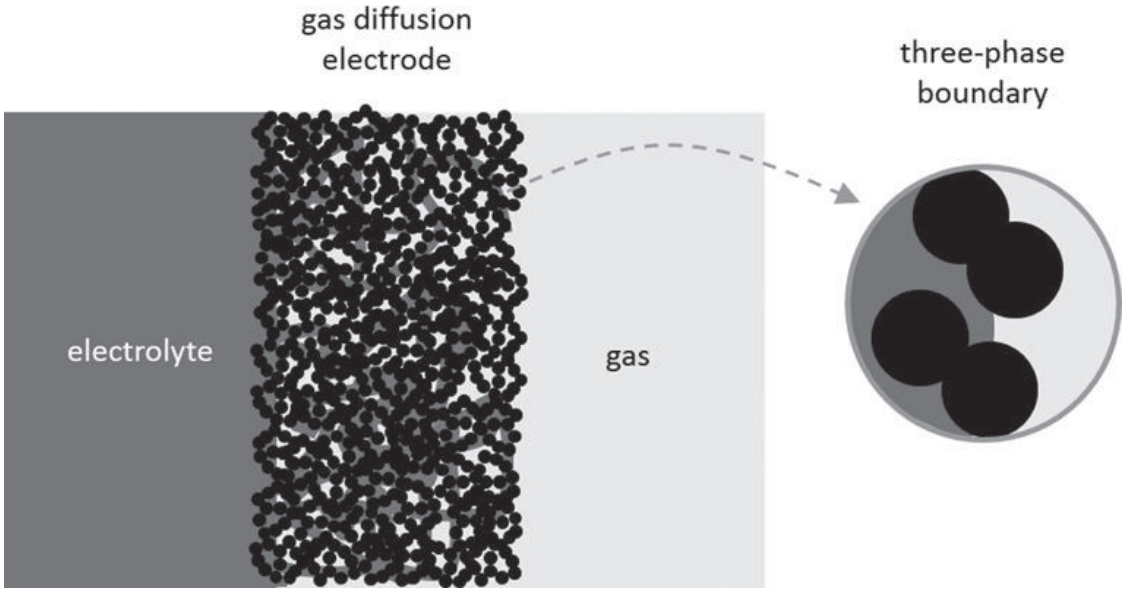

Figure 2.5. Schematic representation of Gas diffusion electrode (Kubannek, 2019)

As a solid phase, the electrode material serves as both an electron conductor and a catalyst, allowing the actual reaction to take place (Hernandez-Aldave, 2020).

The electrolyte, which is typically liquid, serves as both an ion conductor and a reaction media, providing soluble starting ingredients such as hydroxide ions. The electrolyte facilitates the movement of charge-balancing ions. (Hernandez-Aldave, 2020).

The gaseous phase and electrolyte must come into contact with the catalyst grains. Therefore, the structure of the electrode must be porous. This necessitates a massive electrochemically active area with a tiny geometric surface area. The chemical reagents need to permeate the pore structure, and the products formed must exit the electrode. This also has an impact on the electrode's water balance (Hernandez-Aldave, 2020).

There are several problems in gas diffusion electrodes of zinc–air batteries: Corrosion of air electrode, stability and longevity, oxygen diffusion, clogging and blockages, electrolyte compatibility, carbonation of electrolyte, and high overpotential. Cathode typically accounts for 60-70% of cell production costs. As a result, the problems that must be tackled grow both more complicated and more severe.

Zinc-air batteries often suffer from corrosion of the air electrode due to the air electrode's exposure to moisture and oxygen during functioning, which causes electrode degradation (Li, 2013). In order to preserve the performance of the battery and lifespan, corrosion prevention is crucial. There are several strategies to prevent this. The air electrode can regulate moisture and lower the danger of corrosion by using hydrophobic materials on the outside and hydrophilic materials on the inside (Lu, 2012). Other than that, the risk of corrosion can be decreased by designing the zinc-air battery with strong sealing mechanisms that keep moisture and other impurities from entering the air electrode (Lee, 2012). Then, the interaction with oxygen and moisture can be managed by adjusting the porosity of the air electrode. Corrosion can be avoided by designing the electrode with optimized porosity (Li, 2013). Due to its exposure to challenging electrochemical conditions, maintaining the stability and lifetime of the air electrode is difficult. As a result, electrode materials may degrade over time (Lee, 2012). The air electrode depends on oxygen diffusing to the electrode surface from the surrounding area. It can be difficult to ensure effective oxygen diffusion, particularly in compact and enclosed battery architectures (Singh, 2018). The performance of the battery can be decreased by particles, dust, and other pollutants clogging or blocking the air passageways, which prevents oxygen from reaching the electrode (Guo, 2017).

In zinc-air batteries, it is crucial that the air electrode and the electrolyte work well together. Any mismatch may result in electrode deterioration, which could reduce the battery's capacity (Li, 2013).

The electrolyte can absorb atmospheric carbon dioxide and convert it into carbonates. The air electrode may react with these carbonates and lose effectiveness as a result (Li, 2013). Due to its high surface area, carbon is a widely used substance for metal-air batteries in the part of air electrodes to improve the oxygen reduction reaction activity. However, carbon dioxide in alkaline media forms carbonate compounds that do not dissolve in electrolyte solution, which precipitate and block the active sites of the catalytic surfaces. So capacity loss is inevitable. This type of corrosion shortens the lifetime of the Zn-air batteries. To eliminate this problem, carbon should be removed from the cathode.

Carbon-free air electrodes have started to gain a place in the literature and have become competitive compared to their carbon-based counterparts. The carbon-free air electrodes produced by the electrodeposition method were checked against the commercial carbon air electrodes, and it was observed that the produced air electrodes

gave results close to the commercial ones when the battery cycle life was studied (Bekish, 2020). In addition, for lithium–oxygen batteries, carbon-free $NiCo_2O_4$ electrodes with three-dimensional architectures have been developed using the hydrothermal method. $NiCo_2O_4$ electrodes have exceptional catalytic activity in the oxygen reduction process (ORR). Under a current density of 0.05 mA cm^2, the $NiCo_2O_4$ electrode had a big capacity of 3693.2 $mAh.g^{-1}$ and a decreased over-potential (Yuan, 2019). In another study, self-supported binders and carbon-free electrodes were produced (Wu, 2020). Their setup shows excellent cycle stability over 200 cycles for eight days at 5 $mA.cm^{-2}$. Mainar et al. used $NiCo_2O_4$ as an electrocatalyst in order to compare it with carbon nanotube as an electrocatalyst in an air-electrode. The discharge specific capacity at 2 $mA.cm^{-2}$ is quite similar for secondary zinc-air batteries constructed with c-BAE (carbon-based electrode) (778.53 $mAh.g^{-1}$) and m-BAE (nickel-based electrode) (797.12 $mAh.g^{-1}$) cathodes. However, the coulombic efficiency of a c-BAE secondary zinc-air battery is significantly lower than that of an m-BAE secondary zinc-air battery (51.37% vs. 94.72%). In terms of specific energies, c-BAE delivers 290.38 $Wh.kg^{-1}$, whereas m-BAE zinc-air batteries deliver 242.99 $Wh.kg^{-1}$. The higher specific energy of the c-BAE secondary zinc-air battery is associated with the smaller weight of the carbon-based electrode and the battery's higher discharge voltage. Galvanostatic pulse cycling measurements were carried out at discharge and charged at a current density of 2 mA.cm-2 for 1 hour. Each charge/discharge step was used to assess the stability of secondary zinc-air batteries across continuous charge and discharge cycling. The c-BAE was stable for 88 cycles, but the reversibility of the m-BAE was greater than 2,400 cycles (Mainar, 2023). In other work, Fujiwara et al. synthesized perovskite oxides ($La_{0.6}Ca_{0.4}CoO_3$ (LCCO) and $La_{0.6}Ca_{0.4}MnO_3$ (LCMO) as an electrocatalyst using hydrothermal methods. They put carbon-based and carbon-free perovskite electrodes to the test in order to understand the charge/discharge characteristics. In the beginning, the carbon-based air electrodes demonstrated superior reversibility with lower charge and higher discharge potential than the carbon-free air electrodes. However, the potential of carbon-based electrodes increased and decreased during the charge and discharge processes (Fujiwara, 2022). Martindale et al. created three distinct electrocatalysts made entirely of Fe metal, including FeO_x nanorods, spherical metal Fe nanocrystals, and petal-like FeS_x nanocrystals. These compounds showed remarkably similar activity for OER catalysis, with overpotentials at 10 $mA.cm^{-2}$ all about 400 mV in 0.1 M KOH, and bias potentials of 0.36 V and 1.68 V (vs. RHE, at

10 mA.cm^{-2}) for the HER and OER, respectively (Martindale, 2015). Zhang et al. established a practical anion exchange method for converting 1D Co_3O_4 nanowires into CoP porous nanowires for the OER and HER, which can be powered by a single-cell "AA" battery with overpotentials of 147 mV and 326 mV at a current density of 10 mA.cm-2 for the HER and OER, respectively (2017).

The working principle of zinc-air batteries is based on the energy obtained from oxygen evolution (OER) and oxygen reduction (ORR) reactions. These two reaction mechanisms are continuously repeated during the charging and discharging of the battery. However, a high overpotential is required for the mentioned electrochemical reactions to take place therefore the battery to work. This reduces the energy and power density of the battery, which leads to a decrease in its energy efficiency. There are several electrocatalysts to improve the performance of the OER and ORR. For example, Pt, Pd, Ir, and Ru-based catalysts are currently used (Sun, 2018). However, the abundance and price of these metals challenge the commercialization of Zn-air batteries. However, there are multiple different choices for catalyst materials. For example, metal oxides such as transition metals have the potential as alternatives to these metals.

Manganese oxides are promising materials to be used in air electrodes in zinc-air batteries. Particularly for the oxygen reduction reaction (ORR) and oxygen evolution reaction (OER), which are critical activities in zinc-air batteries, manganese oxides demonstrate significant electrocatalytic activity. Their catalytic activity aids in improving the battery's overall performance. Manganese oxides are widely available and reasonably priced materials. Due to their low cost, they are desirable alternatives for large-scale energy storage applications since they can assist in lowering the price of zinc-air batteries. In addition, manganese dioxide is one of the manganese oxides that is well-known for its chemical stability in the aqueous setting of zinc-air batteries. The battery's longevity and cyclability are both increased by this stability. Also, manganese oxides are thought to be environmentally benign. The sustainability of energy storage systems can be improved by using them in batteries instead of more expensive and potentially harmful catalysts (Mainar, 2018).

There are several synthesis routes to obtain Mn_xO_y, such as the co-precipitation method, hydrothermal synthesis, sol-gel method, electrodeposition, and redox method. The co-precipitation method is one of the commonly used methods for Mn_xO_y synthesis. Precipitation has multiple advantages through the synthesis, such as fast and controlled preparation, ease of particle size control, etc. This method can employ different

manganese salts such as $KMnO_4$, $MnSO_4$, $C_6H_9MnO_6{\cdot}2H_2O$. Choi et al. (Choi 2014) used this method and obtained mesoporous MnO_2. Their MnO_2 electrodes showed stable performance at 700 $mAhg^{-1}$. Another common method is redox reactions. Popular precursors for this route are MnO_4^- and Mn^{2+} (Bach, 1990). The other method used for the synthesis of MnxOy is the hydrothermal route. The hydrothermal method is a cost-effective and simple route for Mn_xO_y synthesis. However, it has the disadvantage of poor crystallinity of the final product (Feng, 2014). Xu et al. (Xu, 2016) synthesized hybrid nanocomposite for Mn_xO_y derivative electrocatalyst and observed that their battery showed satisfactory performance at 970 $mAhg^{-1}$. Li et al. (Li, 2015) synthesized carbon black/manganese composite air electrode for zinc-air batteries and found out that the battery showed satisfactory performance at 798 $mAhg^{-1}$. Mainar et al. (Mainar, 2016) synthesized different manganese oxides using thermal methods. Their most promising α-MnO_2 catalyst was put through testing in a rechargeable Zn-air battery cell, demonstrating more than 200 charge/discharge cycles, capacity retention above 95%, and round-trip efficiency of around 53%. Fujimoto et al. (Fujimoto, 2020) doped cobalt into the γ-MnO_2 framework, and electrolytic manganese oxide was changed into a bifunctional catalyst for both the oxygen evolution process and the oxygen reduction reaction. The method entails treating electrolytic manganese dioxide wetly while N_2H_4 and Co^{2+} are present. Electrolytic manganese dioxide is inherently active for the ORR rather than the OER. A remarkably high mass activity for the OER was demonstrated by a small quantity of Co substitution, although it had no effect on the pristine EMD's ORR properties. The overpotential in the OER was measured to be 440 mV at 10 mA cm-2 and 447 mV at -1 mA cm^{-2}. Their sum of 887 mV was similar to that of Pt/C and significantly lower than the pristine EMD's (1040 mV). Han et al. used cathodic polarization in $NaPO_2H_2$ solution to create an amorphous Mn-Co-P layer on $MnCo_2O_4$ supported on a titanium mesh. The catalyst exhibited an of 0.269 V in an alkaline medium at a current density of 10 $mA.cm^{-2}$, Tafel slope of 102 $mV.dec^{-1}$ (Han, 2018).

In addition to manganese-based oxides, the use of nickel and cobalt-based oxides, which are also among the transition metals, increases the bifunctionality of the catalyst. Also, due to their significant corrosion and instability in acidic medium, nickel-based catalysts operate better in alkaline circumstances than in acidic conditions (Zaiman, 2023). Chen et al. discovered that following heat treatment with NH_3 at 200°C, $NiCoO_{x-2}$ nanosheets give an OER current density of 10 $mA.cm^{-2}$ at a low overpotential of 239 mV (Chen, 2023). Li et al. described an air electrode made of a Ni-

based catalyst and GDL, as well as material in the form of Ni powder and Ni foam. The authors claimed that nickel air electrodes have good long-term durability at a recharge potential of 0.55 V vs. Hg/HgO and a high current density of 100 $mA.cm^{-2}$ (Li, 2013). Han et al. used anisotropic chemical etching to create Ni-Co mixed oxide nanocages using Ni-Co metal-organic framework precursors. They displayed low overpotential (0.380 V@10 $mA.cm^{-2}$) and Tafel slope (50 $mV.dec^{-1}$) under basic medium thanks to their 3-D cage-like hollowed structure and high surface area to volume ratio (Han, 2016).

Hao et al. prepared nickel-cobalt oxides supported on Co/N decorated graphene. Their catalyst $Ni_xCo_yO_4$/Co-NG composite showed great electrochemical performance in both ORR and OER. Tafel plots were used to investigate the OER kinetics of these samples. The slope of NixCoyO4/Co-NG was 77.2 mV/dec (Hao, 2017). Qi et al. created an orientated assembly out of hexagonal $Co(OH)_2$ nanosheets. For increased durability, their assembled configuration can help avoid the aggregation and ripening that occurs during electrolysis. The nanosheet assembly could produce 10 $mA.cm^{-2}$ current density at an overpotential of 0.359 V, while the isolated nanosheet required an overpotential of 0.394 V to obtain the same current density. Furthermore, when measured by LSV at 5 $mV.s^{-1}$, the nanosheet assembly displays a Tafel slope of 76 $mV.dec^{-1}$. This value is lower than that shown by the separated nanosheets (95 $mV.dec^{-1}$) (Qi, 2019). Lu et al. and colleagues created a nanowire array of nickel and cobalt oxides that stood freely on a nickel foam substrate ($Ni_xCo_{3-x}O_4$-1:1). They discovered that doping the Co_3O_4 with Ni increased the roughness, which boosted the activity of the catalyst. Electrochemical experiments revealed overpotential values of 0.56 V and 0.65 V at 5 $mA.cm^{-2}$ for $Ni_xCo_{3-x}O_4$-1:1 and Co_3O_4, respectively. At 0.6 V, the current density of $Ni_xCo_{3-x}O_4$-1:1 was approximately 5 times that of pure Co_3O_4. After 10 hours in an alkaline medium, the stability test revealed a minor change in potential. The existence of a large active electrochemical surface area for enhanced charge conduction results in small Tafel slopes, decreased overpotential, and high current density (Lu, 2011). Liang et al. created 2-dimensional ultrathin α-$Co(OH)_2$ nanosheets using a straightforward preparation procedure. At room temperature, an aqueous solution of cobalt salt was mixed with a methanolic solution of 2-methylimidazole. The thin structure of the catalyst enabled the α-$Co(OH)_2$ nanosheet to function exceptionally well for OER. The obtained material has an overpotential value of 0.267 V at j=10 $mA.cm^{-2}$. Furthermore, the Tafel slope of the α-$Co(OH)_2$ nanosheets was 64.9 $mV.dec^{-1}$. This is less than that of

commercial RuO2 (78.7 $mV.dec^{-1}$) and hexagonal α-$Co(OH)_2$ plates (81.2 $mV.dec^{-1}$) (Liang, 2019).

CHAPTER 3

MOTIVATION

In Chapter 3, the motivation of the research is investigated. The main purpose of the work is to synthesize the electrocatalyst for the air electrode of zinc-air batteries within the scope of the M-Era.NET “AMAZE” 2020 Project.

3.1. Carbon-free Catalyst Layer

Carbon in the catalyst layer of the air electrode causes several problems, such as carbon corrosion and clogging of pores.

Carbon-based materials, such as graphite or carbon black, are frequently employed in air electrodes as supports and for increasing conductivity. However, carbon corrosion can happen over time in the hostile alkaline environment of zinc-air batteries. A reduction in the battery's overall performance and efficiency might be caused by carbon corrosion. It might lead to a decrease in the carbon's catalytic activity, which would impact the oxygen reduction reaction.

In addition to that, the porous nature of carbon compounds generally helps to facilitate the oxygen reduction process. Nevertheless, the performance of the electrode may be impacted as these pores fill with reaction products over time. Then, decreased porosity may restrict oxygen's ability to reach the carbon electrode's active sites, which would lower battery performance overall, especially with regard to power density (Ng, 2017).

So, it can be said that zinc-air batteries can be benefitted from carbon-free air electrodes.

3.2. Bifunctional Catalyst

The rechargeable zinc-air battery operates on the principle of a chemical power supply consisting of a metal anode and an air cathode, which are oxygen reduction and oxygen evolution processes, respectively, the discharging and charging reactions in the air electrode. The ORR and OER reactions' reversibility is critical in deciding the performance of the air electrode, hence, the zinc-air battery. Because of the high potential difference between the ORR and OER, as well as their complex processes, highly effective bifunctional ORR and OER catalysts are required to address their slow kinetic difficulty (Deng, 2022).

The production of high-performance bifunctional ORR/OER catalysts is required for increasing the efficiency and stability of zinc-air batteries. At the moment, Pt-based catalysts are thought to have outstanding ORR characteristics, whereas Ru and Ir-based precious metal catalysts have optimum OER catalytic activity. However, the high cost of precious metal catalysts limits their economic applicability. As a result, affordable and effective transition metal-based catalysts are crucial to energy research (Zhang, 2022).

Mn-based materials have the potential to be useful as bifunctional electrocatalysts for the ORR and OER. Furthermore, they have been getting a lot of attention due to their inexpensive cost and great operational stability during ORR and OER (Gorlin, 2010). However, it is challenging for a single element and structural catalyst to demonstrate both significant ORR and OER activity. Therefore, other considerations for electrocatalysts must be made. For example, the combined use of nickel and cobalt oxide is used as OER and ORR electrocatalysts (Chen 2023). Using these three transition oxides is a real opportunity to synthesize a bifunctional ORR/OER electrocatalyst.

3.3. Gas Diffusion Layer

The GDL's principal role is to allow oxygen to diffuse from the surrounding air to the air electrode. Because oxygen is one of the reacting agents in the battery, this is required for the electrochemical process to occur.

GDL is porous in nature, with a wide surface area for contact between air and the electrode. This porous structure enables effective oxygen transport, making sure the reaction proceeds quickly enough to provide the appropriate electrical current.

The GDL also aids in electrolyte management. It aids in the maintenance of electrolyte-air electrode balance, avoiding flooding or drying out of the electrode. Proper electrolyte handling is critical for the battery's overall performance and lifetime (Smolinka, 2021).

3.4. AMAZE Project

The AMAZE project is a three-section project that aims to produce rechargeable zinc-air batteries within the scope of the European Green Deal. These batteries have a crucial role in storing energy. These three sections have different roles in the project. IZTECH from Turkey is responsible for producing the cathode, that is, the air electrode. SINTEF from Norway is responsible for the development of the zinc electrode. EASYL from France is responsible for the development of multi-layered electrodes using porous current collectors.

The joint contributions of these three organizations play a significant role in order to achieve the climate-neutral Europe by 2050 targets set by the European Union.

CHAPTER 4

EXPERIMENTAL

4.1. Materials

In this study, Mn_xO_y powders were synthesized using $KMnO_4$ and $MnSO_4.H_2O$ as starting materials. Analytical grade chemicals, $KMnO_4$ (Merck, 7722-64-7), $MnSO_4.H_2O$ (Sigma Aldrich, 10034-96-5), $NiSO_4$ and $CoSO_4.7H_2O$ (10026-24-1) NaOH (Sigma Aldrich, 1310-73-2), 37 (v/v)% HCl solution (Sigma Aldrich, 7647-01-0) were used for preparation of Mn_xO_y and $Mn_xNi_yCo_zO_t$ powders in the study. MnO_2 (Sigma Aldrich, 1313-13-9) and TiO_2 (Sigma Aldrich) were used for air electrode preparation.

4.2. Methods

4.2.1. Mn_xO_y Synthesis at Different pH Values

Mn_xO_y powders were synthesized using $KMnO_4$ as the precursor. The aim of this section was to analyze the effect of different pH values (0.20, 2, 7, 9.5 and 12) on morphology, surface area, phases and electrochemical properties of synthesized Mn_xO_y powders. The precipitation method was used for Mn_xO_y synthesis. 12 M 37% HCl solution was slowly added to 1 M $KMnO_4$ solution for 30 minutes of constant stirring at 500 rpm. A 12 M NaOH solution was used to change the pH of the reaction medium. After that, a centrifuge (Sigma 3-16 PK) was used to separate solid particles. The mixture was centrifuged three times at 8000 rpm for 10 minutes and washed with deionized water. Finally, the particles were washed with ethanol and centrifuged at 8000

rpm for 5 minutes one more time. After that, the solid Mn_xO_y was dried at 120°C for 1 hour. Dry Mn_xO_y particles were annealed at 350°C for 2 hours (with 10°C/min heating/cooling rate).

4.2.2. Mn_xO_y Synthesis at Different Temperatures

Mn_xO_y powders were synthesized using $KMnO_4$ and $MnSO_4.H_2O$ as precursors. The aim of this section was to analyze the effect of temperature (20°C, 45°C and 60°C) on morphology, surface area, phases and electrochemical properties of synthesized Mn_xO_y powders. The same method mentioned earlier in the *"Mn_xO_y Synthesis at Different pH Values"* section was used. The only difference was the addition of 2 M NaOH to the MnSO4.H2O solution for 2 hours under constant stirring of 500 rpm to the reaction medium when MnSO4.H2O was used as a precursor.

4.2.3. Mn_xO_y Synthesis with Different Precursors

Mn_xO_y powders were synthesized using $KMnO_4$ and $MnSO_4.H_2O$ as precursors. The aim of this section is to evaluate the effect of different precursors at the same temperature and pH values. The same procedure mentioned earlier in the *"Mn_xO_y Synthesis at Different pH Values"* and *"Mn_xO_y Synthesis at Different Temperatures"* sections was followed.

4.2.4. $Mn_xNi_yCo_zO_t$ Synthesis

$Mn_xNi_yCo_zO_t$ powders were synthesized using $KMnO_4$ $NiSO_4$ and $CoSO_4.7H_2O$ as precursors. The precipitation method was used for $Mn_xNi_yCo_zO_t$ synthesis. 12 M 37% HCl solution was slowly added to a mixture of 0.1 M KMnO4, 0.05 M NiSO4, and

0.025 M $CoSO_4.7H_2O$ solution for 30 minutes of constant stirring at 500 rpm. A 12 M NaOH solution was used to change the pH of the reaction medium. After that, a centrifuge (Sigma 3-16 PK) was used to separate solid particles from the mixture. The mixture was centrifuged three times at 8000 rpm for 10 minutes and washed with deionized water. The final wash was carried out with ethanol, and the mixture was centrifuged at 8000 rpm for 5 minutes. Solid $Mn_xNi_yCo_zO_t$ was dried at 120°C for 1 hour. Dry Mn_xO_y particles were annealed at 350°C for 2 hours (with 10°C/min heating/cooling rate).

4.2.5. Physical and Morphological Characterization

Scanning Electron Microscopy (SEM) was used to evaluate the morphology of the catalysts using the FEI Quanta250 system equipped with a field emission gun. Energy-dispersive X-ray Spectroscopy (EDX) was used to analyze the chemical composition of the catalyst powder. Brunauer – Emmett – Teller (BET) method was used to analyze the surface area of synthesized manganese oxides using the Quantochrom Autosorb-1 system. Samples were degassed at 190°C for 5 minutes and cooled for 7 hours under vacuum. X-ray diffraction (XRD) was used to investigate the crystalline structure of manganese oxides, using a Phillips^{TM} Xpert diffractometer with Cu Kα radiation source. Data were collected in the 2θ range of 10-80° with a constant scanning speed of 0.8θ/s.

4.2.6. Electrode Preparation

Ni-mesh current collectors were cut into rectangular shapes with 3 cm x 5 cm dimensions. Ultrasonic treatment was carried out in acetone for 30 minutes and in 2M HCl for 50 minutes, respectively. Current collectors were then dried at 120°C for 1 hour. After that, the catalyst paste was prepared with a 70:30 (catalyst/TiO2) weight ratio, and the sample was wetted with 2-3 mL of 6 M KOH solution. The catalyst paste was then

spread onto current collectors. The catalyst and current collector were pressed together at 100 bar for 5 minutes using a hydraulic press. The sample was partially dried at 80°C for 30 minutes before annealing at 350°C for 2 hours. Finally, the gas diffusion layer was pressed onto the catalyst layer using a hydraulic press at 100 bar for 5 minutes.

4.2.7. Electrochemical Characterization

For the characterization of air electrodes, cyclic voltammetry and linear sweep voltammetry measurements were carried out using a three-electrode setup with fabricated air electrodes as working electrodes, Pt wire as counter electrode, and Ag/AgCl as reference electrode connected to a Gamry Model 1010B Potentiostat. Cyclic voltammetry was used to investigate current densities of air electrodes in the range of -1 and 1.5V with a scan rate of 5mV/s. Linear sweep voltammetry was used to determine the onset potentials of air electrodes in the range of -1.5 and 1.5V with a scan rate of 5mV/s. Tafel plots were also generated using the same settings. Tafel plots show the relationship between the current generated in an electrochemical cell and the electrode potential of a specific metal. Finally, the charge-discharge cycles were used to determine the voltage capacity of the air electrodes, and how they contain their voltage capacity in time. Additionally, the electrochemical analysis processes were carried out with a half-cell setup. When we consider half-cell and full-cell battery installations, in half-cell setups, results are obtained corresponding to the reference electrode, not the anode. For this reason, the performance of the electrode is close to ideal. However, in full-cell setups, the obtained results are in order to anode. Taking this into consideration in the future stages of the study, tests with full-cell setups should also be added to the study.

4.3. Experimental Matrix

The parameters investigated and sample names are given below in Table 4.1.

Table 4.1. Experimental Matrix

	HCl ratio	pH	Temperature	Precursor	Volumetric ratio
(K)MnO_2-20:2	x				
(K)MnO_2-20:4	x				
(K)MnO_2-pH2		x			
(K)MnO_2-pH12		x			
(K)MnO_2(20:4)-pH9.5@20°C			x	x	
(K)MnO_2(20:4)-pH9.5@45°C			x	x	
(K)MnO_2(20:4)-pH9.5@60°C			x	x	
(S)MnO_2-pH9.5@20°C			x	x	
(S)MnO_2-pH9.5@45°C			x	x	
(S)MnO_2-pH9.5@60°C			x	x	
(K)$Mn_xNi_yCo_zO_t$(1:1:1)-pH9.5@60°C				x	x
(K)$Mn_xNi_yCo_zO_t$(1:0.5:0.5)-pH9.5@60°C				x	x
(S)$Mn_xNi_yCo_zO_t$(1:1:1)-pH9.5@60°C				x	x
(S)$Mn_xNi_yCo_zO_t$(1:0.5:0.5)-pH9.5@60°C				x	x

4.4. Synthesis Method Visual

The experimental procedure, which includes synthesis of catalyst particles, air electrode preparation, and testing, is illustrated below in Figure 4.1.

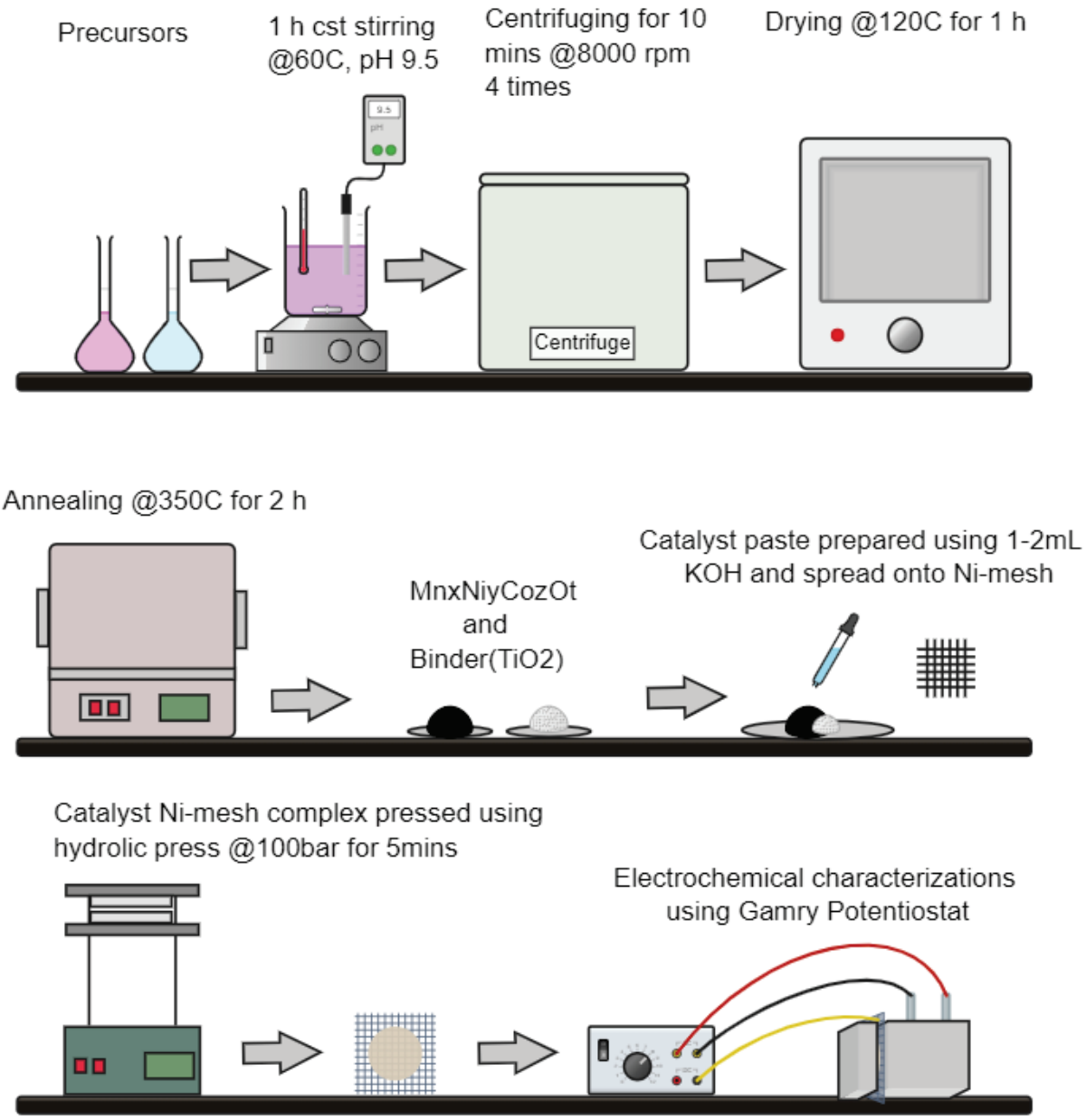

Figure 4.1. Synthesis Method

CHAPTER 5

RESULTS AND DISCUSSION

In Chapter 5, the structural and electrochemical characterization of air electrodes are investigated in detail.

5.1. Effect of HCl Amount

Figure 5.1. (a) and (b) shows SEM images of (K)Mn_xO_y-20:2 and (K)Mn_xO_y-20:4 catalysts, respectively. (K)Mn_xO_y-20:2 sample shows a well-dispersed uniform amorphous nanoneedle-like and aggregated structures similar to the previously observed structures by King'ondu et al. (King'ondu, 2011). They produce self-assembled multidope cryptomelane hollow microsphere γ-MnO_2 with small particles (4-6 nm) using multiple framework substitutions. In addition to that, the (K)MnxOy-20:2 sample showed homogeneous particle size distribution, and the (K)Mn_xO_y-20:4 sample showed uniform amorphous structure with agglomerated behavior. On the other hand, particle size distribution looks less homogenous than the (K)Mn_xO_y-20:2 sample. Also, it should be mentioned that the particle sizes of samples are different. Both reactions take. ace under strong acidic conditions(pH~0.2). Other than that, the only difference is the amount of HCl solution that is used in the reaction. The amount of HCl solution has been doubled by volume in (K)MnxOy-20:4. So that as the HCl amount increases, the average particle size decreases. The intensity of peaks from XRD spectra supports this claim. HCl amount, therefore acidity, and particle size are directly related to each other.

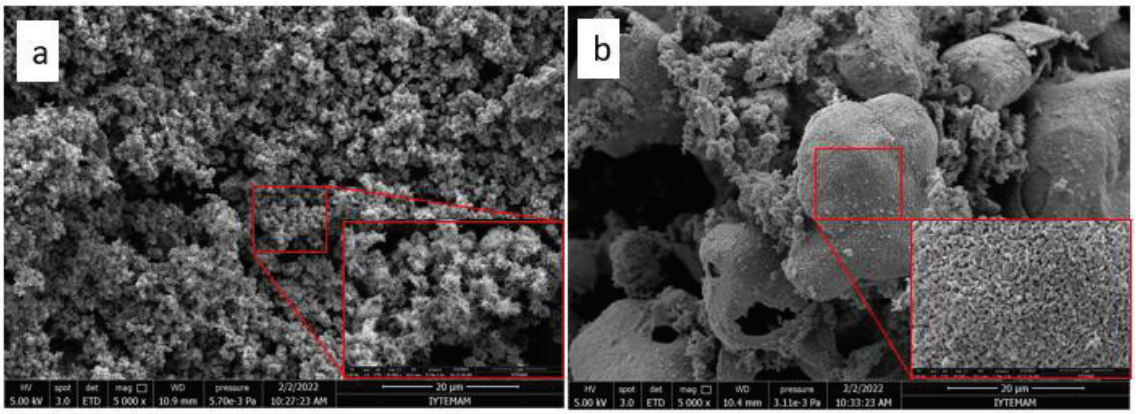

Figure 5.1. SEM images of (a) (K)Mn_xO_y-20:2 and (b) (K)Mn_xO_y-20:4

Figure 5.2. shows the XRD spectra of (K)Mn_xO_y-20:2 and (K)Mn_xO_y-20:4 samples. Peaks at the 12.7°, 18°, 28.8°, 37.5° and 42.1° can be attributed to α-MnO_2(Feng et al. 2014). Peaks at the 23.1°, 33°, 38°, 45.2°, 49°, 55°, 64.2° and 65.8° can be attributed to Mn_2O_3(Yang et al. 2014). Peaks at the 53°, 60°, 67.5° and 69° can be attributed to Mn_3O_4(Ahmed et al. 2014). As the particle size decreases, surface area will increase. The work of Rout et al. (Rout, 2018) and BET results support this claim. This means there are more active sites where reactions occur. Therefore, smaller particle size is a desirable property for a catalyst.

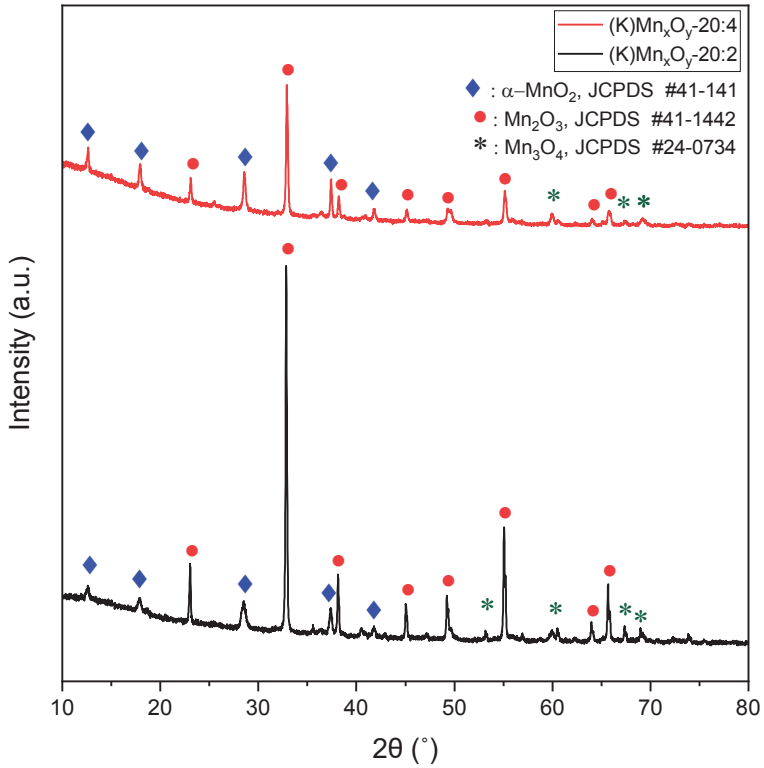

Figure 5.2. XRD spectra of (K)Mn_xO_y-20:2 and (K)Mn_xO_y-20:4 samples

Table 5.1. shows the chemical composition of samples regarding HCl amount as a variable parameter using the Rietveld Refinement Method. Although the dominant manganese oxide phase in the samples is Mn_2O_3, the simultaneous presence of both α-MnO_2 and Mn_2O_3 is theoretically better for enhancing both oxygen reduction reaction and activity of battery (Augustine et al., 2015; Nawaz et al., 2016). The dominant manganese oxide phase in the samples is Mn_2O_3.

Table 5.1. Chemical composition of samples regarding HCl amount as variable

Precursor	Sample Name	pH	Temperature, °C	α-MnO_2(%)	Mn_2O_3(%)	Mn_3O_4(%)
$KMnO_4$	(K)Mn_xO_y(20:2)	0.20	20	9	86	5
$KMnO_4$	(K)Mn_xO_y(20:4)	0.20	20	20	72	8

Table 5.2. shows the BET results for samples. The results shown in the table are expected in the literature (Mohd Yusof et al., 2018). The only difference between (K)Mn_xO_y-20:2 and (K)Mn_xO_y-20:4 samples is the amount of HCl used during the reaction. From this perspective, it can be said that the HCl amount is directly affecting the surface area. In addition to that, the average pore diameter was doubled between the samples. It can be caused by different particle sizes of (K)Mn_xO_y-20:2 and (K)Mn_xO_y-20:4 due to the HCl amount. This also can be observed from SEM images of samples.

Table 5.2. BET characterization results for (K)MnO_2-20:2, (K)MnO_2-20:4

Sample	BET Surface Area, m^2g^{-1} (S_{BET})	Micropore Area, m^2g^{-1} (S_μ)	Total Pore Volume, cm^3g^{-1} (V_P)	Average Pore Diameter, nm ($d_{average}$)
(K)Mn_xO_y-20:2	6.23	5.45	0.0028	9.48
(K)Mn_xO_y-20:4	21.64	1.12	0.0005	4.67

The chosen HCl parameter for further work is 20:4($KMnO_4$:HCl) by volume.

5.2. Effect of pH

Figure 5.3(a), (b), (c), and (d) shows the SEM images of (K)Mn_xO_y-pH2, (K)Mn_xO_y-pH7, (K)Mn_xO_y-pH9.5@20°C and (K)Mn_xO_y-pH12 respectively. The pH effect on morphology was observed. In order to control the pH, 12 M NaOH solution is used. The images clearly show that the particles were significantly agglomerated in nature for (K)Mn_xO_y-pH2 and (K)Mn_xO_y-pH7 samples. Some bigger particles exist as a result of the agglomeration or overlapping of smaller particles. Work of Sagadevan et al (Sagadevan, 2015). Supports this idea. The SEM images clearly reveal randomly distributed grains of varying sizes. However, when the pH value increases to 7 and 9.5, little crystal structures are observed. And in addition to that, while the pH value is 12,

obvious crystals are visible in the images. So, it can be clearly said that increasing pH value increases crystallinity (Lamdab, 2018). The average particle size increases with the increase in pH value. Lamdab et al. investigated the effect of a pH-controlled co-precipitation process while synthesizing $MnFe_2O_4$ nanoparticles.

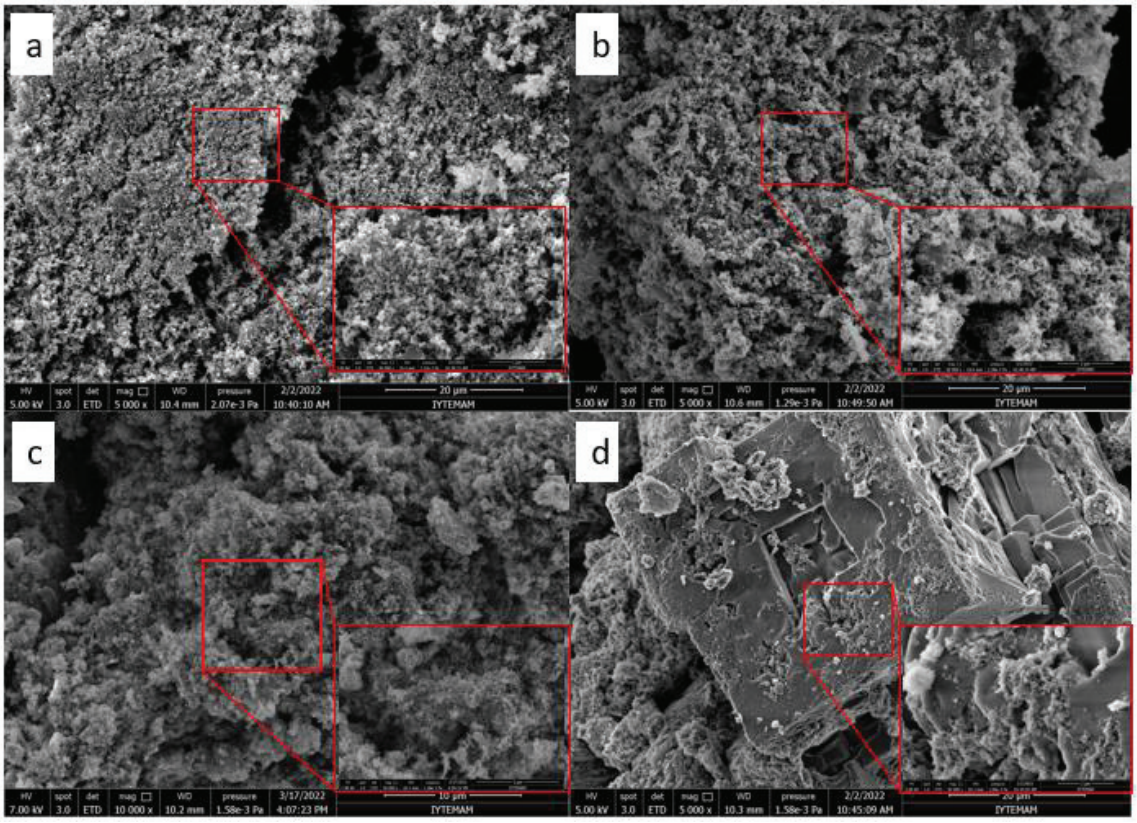

Figure 5.3. SEM images of (a) (K)Mn_xO_y-pH2, (b) (K)Mn_xO_y-pH7, (c) (K)Mn_xO_y-pH9.5@20°C and (d) (K)MnO_2-pH12

Figure 5.4. shows the XRD results of (K)Mn_xO_y-pH2, (K)Mn_xO_y-pH7, (K)Mn_xO_y-pH9.5@20°C and (K)Mn_xO_y-pH12 samples. (K)Mn_xO_y-pH2 sample shows only broad peak at 37.5° and that can be attributed to α-MnO_2(Feng et al. 2014). (K)MnO_2-pH7 sample shows peaks at 28.8° and 37.5° which can be attributed to α-MnO2(Feng et al. 2014), and 31° and 45°, which can be attributed to Mn_2O_3(Yang et al. 2014). (K)Mn_xO_y-pH9.5@20°C sample shows 12.7°, 28.8° and 37.5° those can be attributed to α-MnO_2(Feng et al. 2014). (K)Mn_xO_y-pH12 sample shows 28.8° and 37.5° which can be attributed to α-MnO2(Feng et al. 2014), and 31° and 45°, which can be attributed to Mn_2O_3(Yang et al. 2014).

According to SEM images, crystallinity seems to be increasing with pH; however, based on XRD spectra, the highest crystallinity (sharper peaks) is obtained at pH 7. The conclusion that can be drawn here is that SEM images reflect a very small area of the sample when compared to bulk XRD analysis. For this reason, crystallinity interpretation should be made according to XRD results.

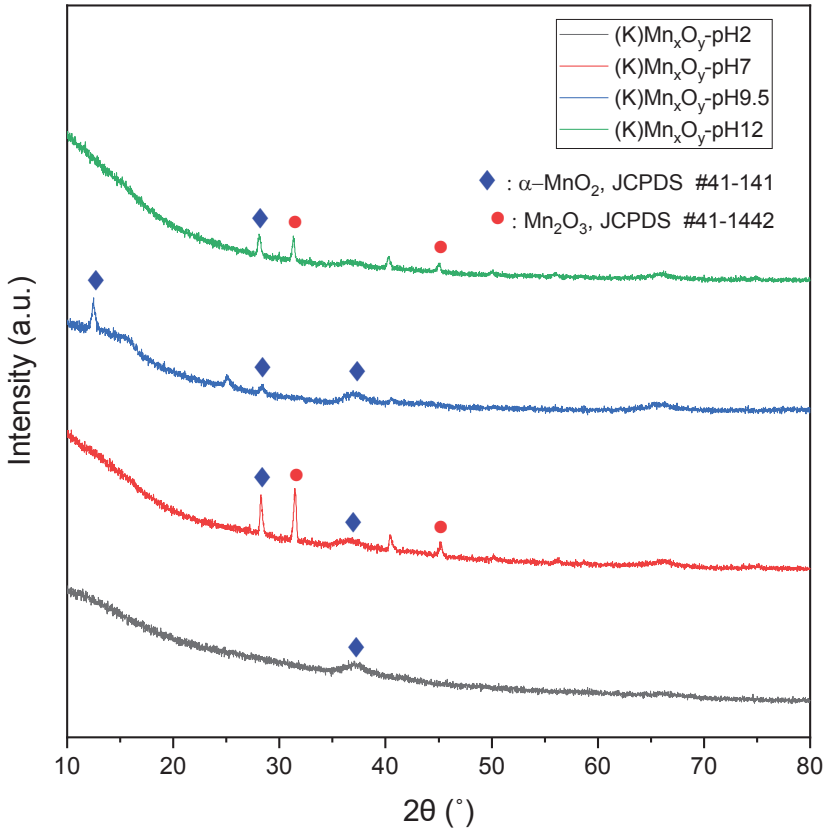

Figure 5.4. XRD spectra of (K)Mn_xO_y-pH2, (K)Mn_xO_y-pH7, (K)Mn_xO_y-pH9.5@20°C and (K)Mn_xO_y-pH12

Table 5.3. shows the chemical composition of samples regarding pH as a variable parameter using the Rietveld Refinement Method. Dominant phase in the samples α-MnO_2 except for sample (K)Mn_xO_y-pH12. As mentioned before, α-MnO_2 enhances the cell activity.

Table 5.3. Chemical composition of samples regarding pH as a variable parameter

Precursor	Sample Name	pH	Temperature, °C	α-MnO_2(%)	Mn_2O_3(%)
$KMnO_4$	(K)Mn_xO_y-pH2	2.0	20	100	0
$KMnO_4$	(K)Mn_xO_y-pH7	7.0	20	68	32
$KMnO_4$	(K)Mn_xO_y-pH9.5@20°C	9.5	20	100	0
$KMnO_4$	(K)Mn_xO_y-pH12	12.0	20	46	54

Table 5.4. shows the BET results of samples. (K)Mn_xO_y-pH12 shows better values compared to (K)Mn_xO_y-pH2. Due to the crystal structure of (K)Mn_xO_y-pH12 shows more surface area as expected (Brousse, 2006). As a result of that, pH has an important impact on surface area. Increasing the pH, increases the surface area. Acidic conditions create roughness on the surface; therefore, the surface area increases (Patungwasa, 2008).

Table 5.4. BET characterization results for (K)MnO_2-pH2 and (K)MnO_2-pH12

Sample	BET Surface Area, m^2g^{-1} (S_{BET})	Micropore Area, m^2g^{-1} (S_μ)	Total Pore Volume, cm^3g^{-1} (V_P)	Average Pore Diameter, nm ($d_{average}$)
(K)Mn_xO_y-pH2	21.66	2.22	0.0011	6.87
(K)Mn_xO_y-pH12	58.10	14.91	0.0076	6.98

5.3. Effect of Temperature

Figure 5.5(a), (b), and (c) shows the SEM images of (S)Mn_xO_y-pH9.5@20°C, (S)Mn_xO_y-pH9.5@45°C and (S)Mn_xO_y-pH9.5@60°C respectively. The majority of the nanoparticles were irregular in form, with some resembling spherical agglomerates, according to SEM images (Sagadevan, 2015). This implies that each grain visible by SEM is composed of many weakly crystalline regions that are displaced from each other

as expected (Brousse, 2006). (S)Mn_xO_y-pH9.5@20°C sample shows agglomerated particles that uniformly dispersed through the surface. Also, (S)MnxOy-pH9.5@45°C and (S)MnxOy-pH9.5@60°C particles show the same agglomerated particles.

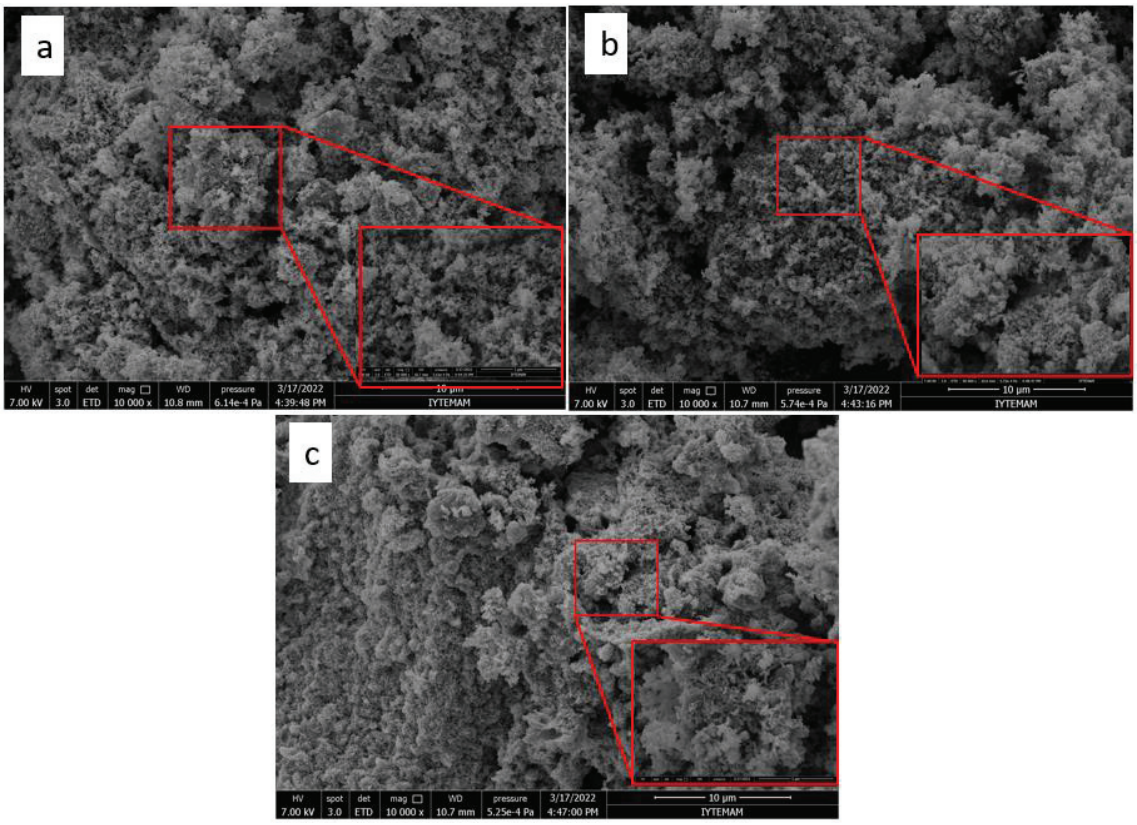

Figure 5.5. SEM images of (a) (S)Mn_xO_y-pH9.5@20°C, (b) (S)Mn_xO_y-pH9.5@45°C and (c) (S)Mn_xO_y-pH9.5@60°C

Figure 5.6. shows the XRD results of (S)Mn_xO_y-pH9.5@20°C, (S)Mn_xO_y-pH9.5@45°C and (S)Mn_xO_y-pH9.5@60°C samples. Peak at 41° can be attributed to α-MnO_2(Feng et al. 2014). Peaks at the 33°, 38°, 49°, 55° and 64.2° can be attributed to Mn_2O_3(Yang et al. 2014). Peaks at 18°, 29°, 31°, 35°, 45°, 51°, 56°, 58.5° and 60° can be attributed to Mn_3O_4(Ahmed et al. 2014). The difference between samples is the changing temperature. As the temperature increases, peak intensities increase. Therefore, crystallinity increases. As the particle size decreases, the surface area should be increased. When the BET results are examined in Table 5.6, it has been observed that the surface area increases as the particle size decreases.

Other than that, the simultaneous presence of these two manganese oxide compounds in the samples may be preferred as an electrocatalyst. The electrochemical characterization will show the results for that.

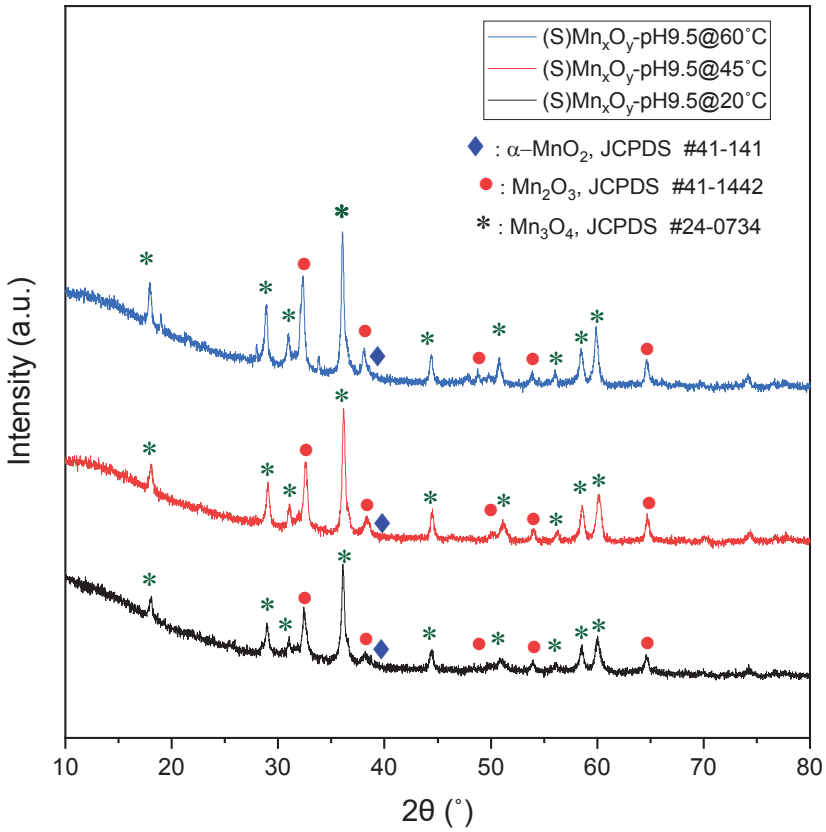

Figure 5.6. XRD spectra of (S)Mn_xO_y-pH9.5@20°C, (S)Mn_xO_y-pH9.5@45°C and (S)Mn_xO_y-pH9.5@60°C

Table 5.5. shows the chemical composition of samples regarding temperature as a variable parameter using the Rietveld Refinement Method. The dominant manganese oxide phase in the sample is Mn_3O_4. The Mn_3O_4 phase of manganese oxide possesses higher OER ability with greater current density and onset potential (Gowda, 2022). Gowda et al. showed that in their work on electrocatalysis OER and ORR activity of ultrathin spinel Mn_3O_4.

Table 5.5. Chemical composition of samples regarding temperature as a variable parameter

Precursor	Sample Name	pH	Temperature, °C	α-MnO_2(%)	Mn_2O_3(%)	Mn_3O_4(%)
$MnSO_4.H_2O$	(S)Mn_xO_y-pH9.5@20°C	9.5	20	1	15	84
$MnSO_4.H_2O$	(S)Mn_xO_y-pH9.5@45°C	9.5	45	1	5	94
$MnSO_4.H_2O$	(S)Mn_xO_y-pH9.5@60°C	9.5	60	4	7	89

Table 5.6. shows the BET results for samples. Samples prepared by using $MnSO_4.H_2O$ as a precursor have significantly low surface area. The reason for this situation can be attributed to the agglomeration of particles on each other. SEM images also support this claim. Surface area increases with increasing temperature as expected, and it is compatible with other samples using KMnO4 as a precursor (Jiangang et al. 2010).

Table 5.6. BET results for (S)Mn_xO_y-pH9.5@20°C, (S)Mn_xO_y-pH9.5@45°C and (S)Mn_xO_y-pH9.5@60°C samples

Sample	BET Surface Area, m^2g^{-1} (S_{BET})	Micropore Area, m^2g^{-1} (S_μ)	Total Pore Volume, cm^3g^{-1} (V_P)	Average Pore Diameter, nm ($d_{average}$)
(S)Mn_xO_y-pH9.5@20°C	11.22	1.91	0.0009	7.03
(S)Mn_xO_y-pH9.5@45°C	15.94	2.40	0.0012	7.05
(S)Mn_xO_y-pH9.5@60°C	17.09	1.91	0.0009	6.61

Figure 5.7(a), (b), and (c) shows the SEM images of (K)Mn_xO_y-pH9.5@20°C, (K)Mn_xO_y-pH9.5@45°C and (K)Mn_xO_y-pH9.5@60°C respectively. (K)Mn_xO_y-pH9.5@20°C sample has uniform amorphous structure. Particles are well dispersed

through the surface, as expected (Sagadevan, 2015). As the temperature rises (K)Mn_xO_y-pH9.5@45°C sample shows better dispersion and slightly bigger particle size due to better nucleation behavior (Loh, 2017). Furthermore (K)Mn_xO_y-pH9.5@60°C sample has the most dispersion among them.

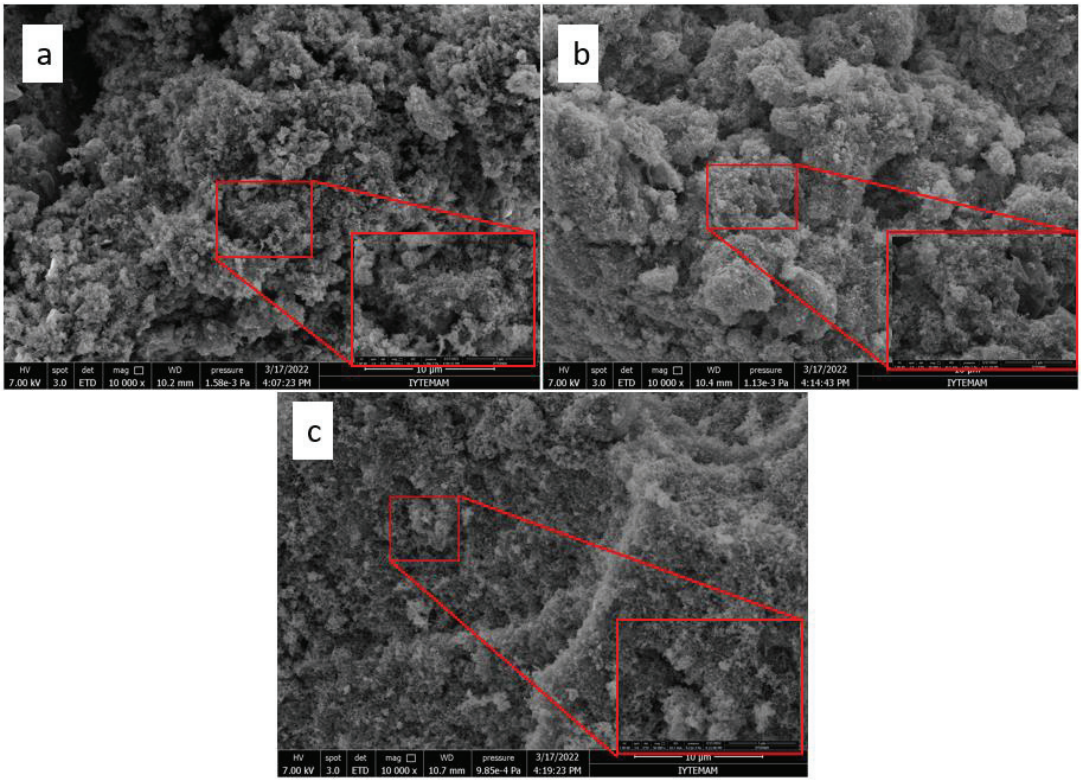

Figure 5.7. SEM images of (a) (K)Mn_xO_y-pH9.5@20°C, (b) (K)Mn_xO_y-pH9.5@45°C and (c) (K)Mn_xO_y-pH9.5@60°C

Figure 5.8. shows the XRD result of (K)Mn_xO_y-pH9.5@20°C, (K)Mn_xO_y-pH9.5@45°C and (K)Mn_xO_y-pH9.5@60°C samples. (K)Mn_xO_y-pH9.5@20°C sample shows 12.7°, 28.8° and 37.5° peaks those can attributed to α-MnO_2(Feng et al. 2014). (K)Mn_xO_y-pH9.5@45°C sample shows peaks at 12.7°, 28.8° and 37.5° which can be attributed to α-MnO2(Feng et al. 2014), and broad peaks at 42° and 65.8° which can be attributed to Mn_2O_3(Yang et al. 2014). (K)Mn_xO_y-pH9.5@60°C sample shows 12.7°, 28.8° and 37.5° which can be attributed to α-MnO2(Feng et al. 2014) and broad peaks at 42° and 65.8° which can be attributed to Mn_2O_3(Yang et al. 2014). However, the intensity of the peaks is different from each other as the temperature changes.

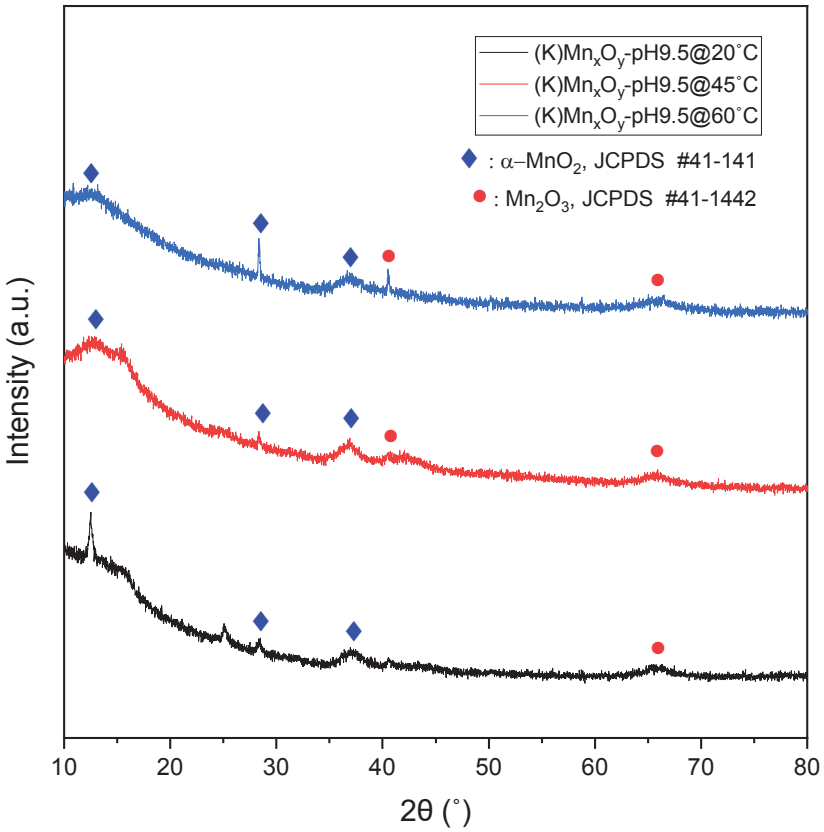

Figure 5.8. XRD spectra of (K)Mn_xO_y-pH9.5@20°C, (K)Mn_xO_y-pH9.5@45°C and (K)Mn_xO_y-pH9.5@60°C

Table 5.7. shows the chemical composition of samples regarding temperature as a variable parameter using the Rietveld Refinement Method. Dominant phase in the samples α-MnO_2. As mentioned before, α-MnO_2 enhances the cell activity.

Table 5.7. Chemical composition of samples regarding temperature as a variable parameter

Precursor	Sample Name	pH	Temperature, °C	α-MnO_2(%)	Mn_2O_3(%)
$KMnO_4$	(K)Mn_xO_y-pH9.5@20°C	9.5	20	78	22
$KMnO_4$	(K)Mn_xO_y-pH9.5@45°C	9.5	45	70	30
$KMnO_4$	(K)Mn_xO_y-pH9.5@60°C	9.5	60	81	19

Table 5.8. shows the BET results for samples. Results regarding the samples prepared by using $KMnO_2$ as a precursor are expected (Mohd Yusof, 2018). The surface area of samples increases with increasing temperature. Because the (K)Mn_xO_y-pH9.5@60°C sample has the best surface area, it is preferable to other samples in catalytic applications.

Table 5.8. BET characterization results for (K)Mn_xO_y-pH9.5@20°C, (K)Mn_xO_y-pH9.5@45°C, and (K)Mn_xO_y-pH9.5@60°C samples.

Sample	BET Surface Area, m^2g^{-1} (S_{BET})	Micropore Area, m^2g^{-1} (S_μ)	Total Pore Volume, cm^3g^{-1} (V_P)	Average Pore Diameter, nm ($d_{average}$)
(K)Mn_xO_y-pH9.5@20°C	55.69	17.73	0.0075	6.17
(K)Mn_xO_y-pH9.5@45°C	58.66	14.27	0.0072	6.01
(K)Mn_xO_y-pH9.5@60°C	85.68	10.40	0.0049	5.83

Selected electrocatalysts for producing air electrodes are (K)MnxOy-20:2, (K)MnxOy-pH9.5@60°C, and (S)Mn_xO_y-pH9.5@60°C. (K)Mn_xO_y-20:2 sample was selected rather than (K)Mn_xO_y-20:4 because of its better dispersion through powder and more uniform structure. (K)Mn_xO_y-pH9.5@60°C and (S)Mn_xO_y-pH9.5@60°C samples are selected among their group with different temperature alternates with 20°C and 45°C because of their better crystal structure and better surface area properties.

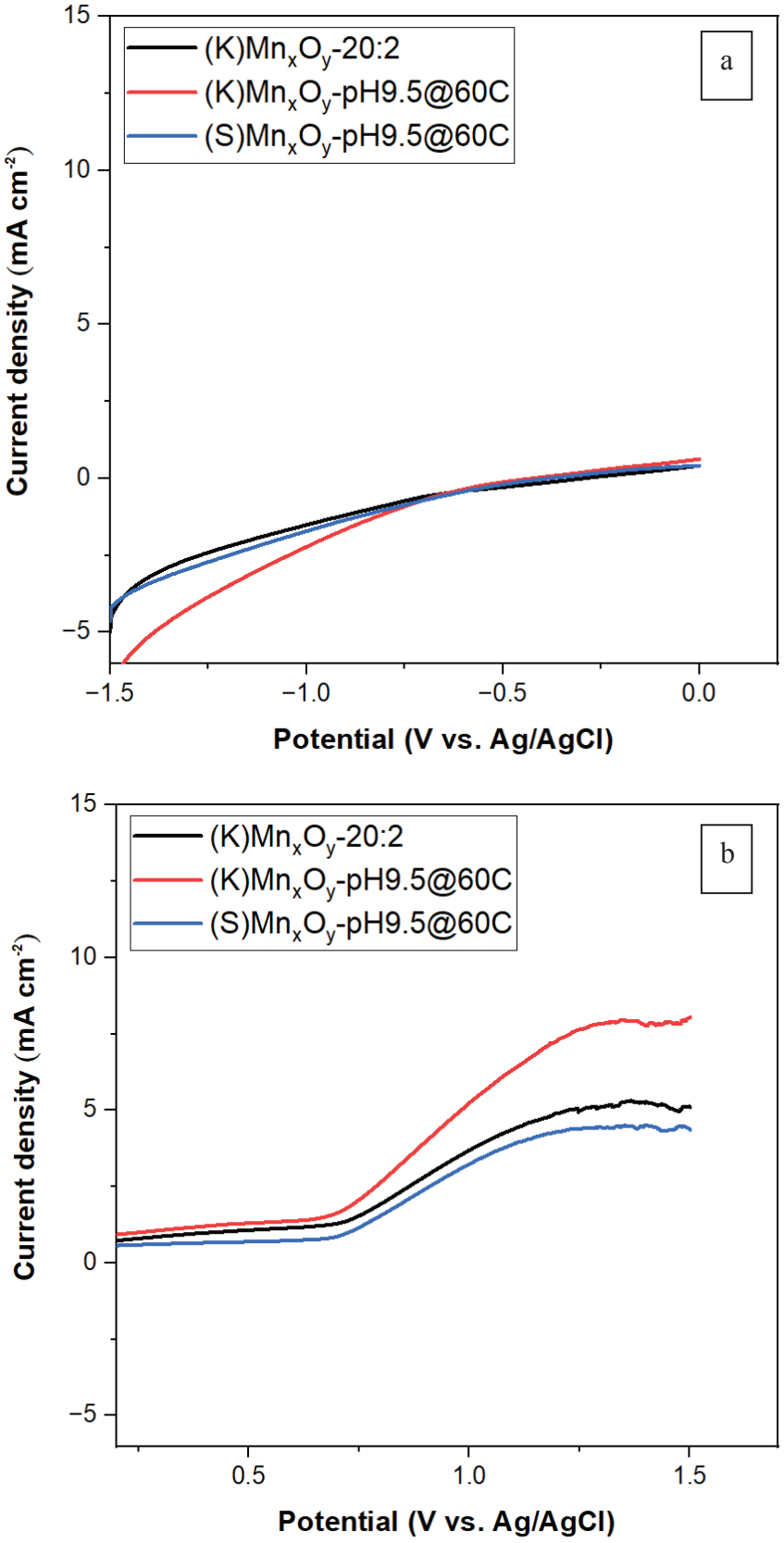

Figure 5.9. Linear sweep voltammograms of (K)Mn_xO_y-20:2, (K)Mn_xO_y-pH9.5@60°C and (S)Mn_xO_y-pH9.5@60°C samples for (a) ORR and (b) OER

Figure 5.9. shows the linear sweep voltammograms of (K)Mn_xO_y-20:2, (K)Mn_xO_y-pH9.5@60°C and (S)Mn_xO_y-pH9.5@60°C samples. (K)Mn_xO_y-pH9.5@60°C shows the best overpotential for oxygen reduction reaction with 650mV and the second best overpotential for oxygen evolution reaction with 271mV among other air electrodes. These results are within the expectations considering previous surface analyses. This sample has both the highest surface area and better catalytic activity. Also, the sample has the most desired manganese oxide phase. In the literature for oxygen reduction reactions, higher overpotential and oxygen evolution reactions with lower overpotential give greater catalytic activity, therefore, more desirable than others (Cheng, 2013), (Ma, 2019). Onset potential values for other electrocatalysts are listed in Table 5.9.

Table 5.9. Onset Potentials of (K)Mn_xO_y-20:2, (K)Mn_xO_y-pH9.5@60°C and (S)Mn_xO_y-pH9.5@60°C samples for ORR

Catalyst	Onset Potential(mV), for ORR	Onset Potential(mV), for OER
(K)Mn_xO_y-20:2	596	231
(K)Mn_xO_y-pH9.5@60°C	650	271
(S)Mn_xO_y-pH9.5@60°C	587	367

Figure 5.10. shows the cyclic voltammograms of (K)Mn_xO_y-20:2, (K)Mn_xO_y-pH9.5@60°C and (S)Mn_xO_y-pH9.5@60°C samples. As can be seen in Figure 5.10. (K)Mn_xO_y-pH9.5@60°C shows the best current density with 10 $mA.cm^{-2}$ among the produced air electrodes. The dominant manganese oxide species is α-MnO_2 for (K)Mn_xO_y-pH9.5@60°C. The sample also has the highest BET surface area with 85.64 cm^2/g. (K)Mn_xO_y-20:2 sample shows the best current density among samples. Dominant manganese oxide species is Mn_2O_3 for (K)Mn_xO_y-20:2. (S)Mn_xO_y-pH9.5@60°C sample shows the lowest current density among samples. The dominant manganese oxide species is Mn_3O_4 for (S)Mn_xO_y-pH9.5@60°C. It can be said that manganese oxide species can be ordered as α-MnO_2 > Mn_2O_3 > Mn_3O_4 for current density. Also, in the literature, the electrocatalytic activities decrease following order α-MnO_2 > Mn_2O_3 > Mn_3O_4(Xue, 2013).

Additionally, a current density of 19 mA.cm^{-2} was measured for commercial manganese dioxide using the same experimental setup indicating that more improvement in electrochemical performance is needed for synthesized manganese oxides.

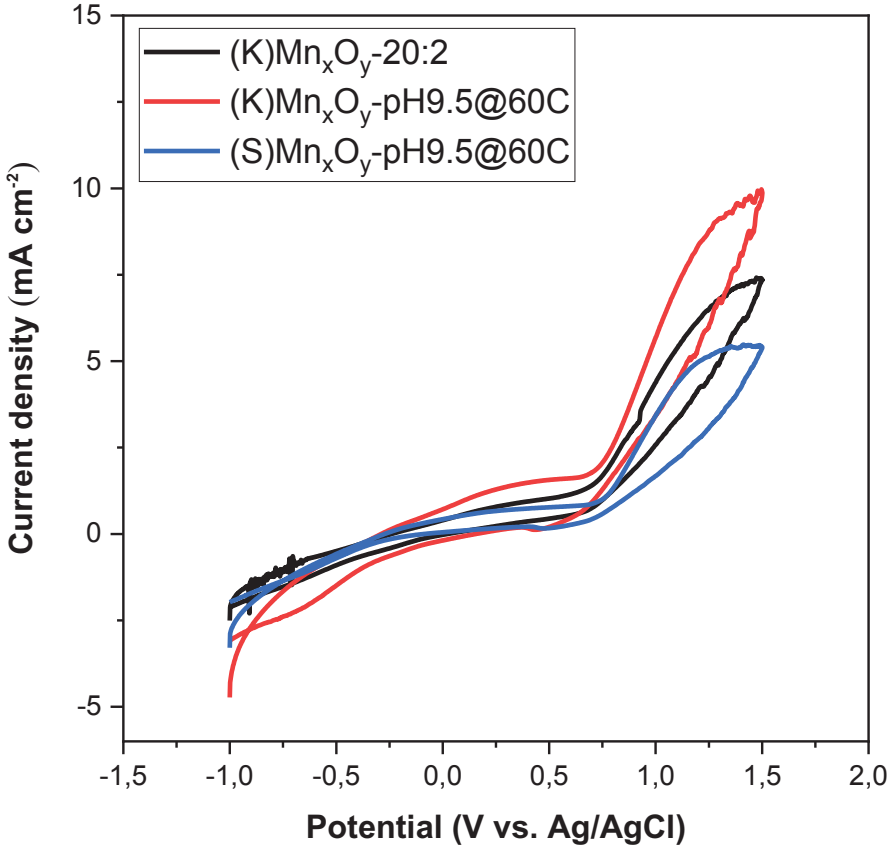

Figure 5.10. Cyclic voltammograms of (K)Mn_xO_y-20:2, (K)Mn_xO_y-pH9.5@60°C and (S)Mn_xO_y-pH9.5@60°C samples

Figure 5.11. shows the Tafel plots for (K)Mn_xO_y-20:2, (K)Mn_xO_y-pH9.5@60°C, (S)Mn_xO_y-pH9.5@60°C and C-MnO_2 catalysts on nickel mesh. Tafel slopes for both ORR and OER are calculated and listed in Table 10. The physical meaning of the Tafel slope indicates how much overpotential must be increased to increase the rate of a reaction. For this reason, a low Tafel slope is a desirable feature. C-MnO_2 shows the best performance in both ORR and OER among other catalysts. However, the difference between values is not so high except (S)Mn_xO_y-pH9.5@60°C for OER. Therefore

(K)Mn_xO_y-20:2, (K)Mn_xO_y-pH9.5@60°C and C-MnO_2 catalysts will show similar performance in this perspective.

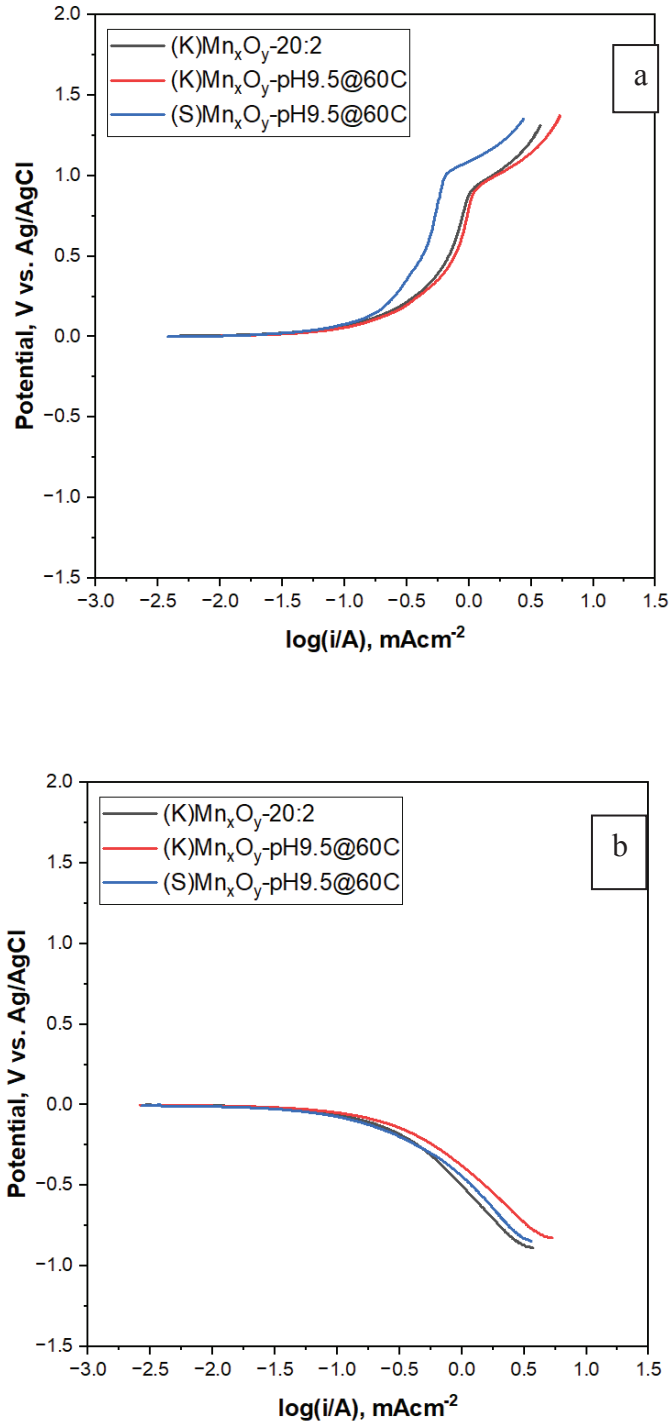

Figure 5.11. Tafel plots of (K)Mn_xO_y-20:2, (K)Mn_xO_y-pH9.5@60°C and (S)Mn_xO_y-pH9.5@60°C catalysts on nickel mesh for (a) OER and (b) ORR

Table 5.10. Tafel slopes of catalysts on Ni-mesh for ORR and OER

Catalyst	Tafel Slope (ORR), mV/dec	Tafel Slope (OER), mV/dec
(K)Mn_xO_y-20:2	34	57
(K)Mn_xO_y-pH9.5@60°C	41	76
(S)Mn_xO_y-pH9.5@60°C	33	106

At this point, (K)MnxOy-pH9.5@60°C catalyst was the best and most promising among all prepared samples due to its Tafel slope, onset potential, and current density results.

5.4. Effect of Precursor and Precursor Concentration

In order to enhance the characteristics(bifunctionality) of the catalyst, 2 other transition metals, nickel and cobalt, were chosen to synthesize a composite metal oxide catalyst, which will be called $Mn_xNi_yCo_zO_t$. Nickel and cobalt were chosen due to their activity on both OER and ORR features (Hao, 2017). The pH and temperature of the reaction media were held constant using previous experimental results, which are 9.5 and 60°C. First of all, different precursors such as $KMnO_4$ and $MnSO_4$ was used to synthesize the catalyst. Then the promising candidates compared with the previous best catalyst (K)Mn_xO_y-pH9.5@60°C.

Figure 5.12. shows the SEM results of (S)$Mn_xNi_yCo_zO_t$(1:0.5:0.5)-pH9.5@60°C and (S)$Mn_xNi_yCo_zO_t$(1:1:1)-pH9.5@60°C samples. It can be clearly seemed that there is amorphous structure rather than a crystalline structure. The particles are in a shape can be said that needle-like and that is an expected structure from this kind of catalyst (King'ondu, 2011). The difference between these two samples is the used precursor ratio during the reaction. Both samples show agglomeration. However, as can be seen when looking at images b and d, the sample (1:1:1) shows a spherical structure compared to the other. This may be due to the increased amount of precursor in the (1:1:1) example.

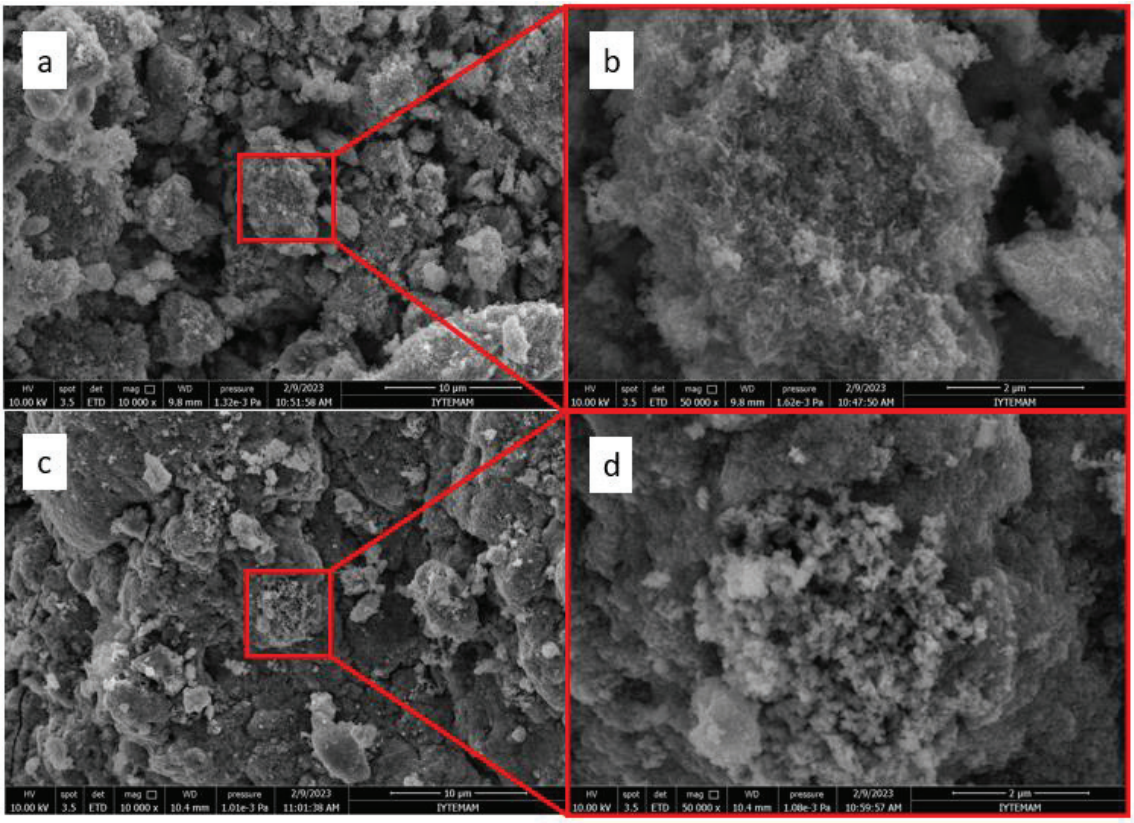

Figure 5.12. SEM images of (S)$Mn_xNi_yCo_zO_t$(1:0.5:0.5)-pH9.5@60°C (a) 10 000x, (b) 50 000x and (S)$Mn_xNi_yCo_zO_t$(1:1:1)-pH9.5@60°C (c) 10 000x, (d) 50 000x

Figure 5.13. shows the SEM results of (K)$Mn_xNi_yCo_zO_t$(1:0.5:0.5)-pH9.5@60°C and (K)$Mn_xNi_yCo_zO_t$(1:1:1)-pH9.5@60°C samples. It can be clearly seen that there is an amorphous structure rather than a crystalline structure. However, these samples have more like spherical shape agglomerates rather than a needle-like structure. These types of particles are also expected from this kind of catalyzer (Sagadevan, 2015). In addition to that, the particle sizes of the samples are similar to each other.

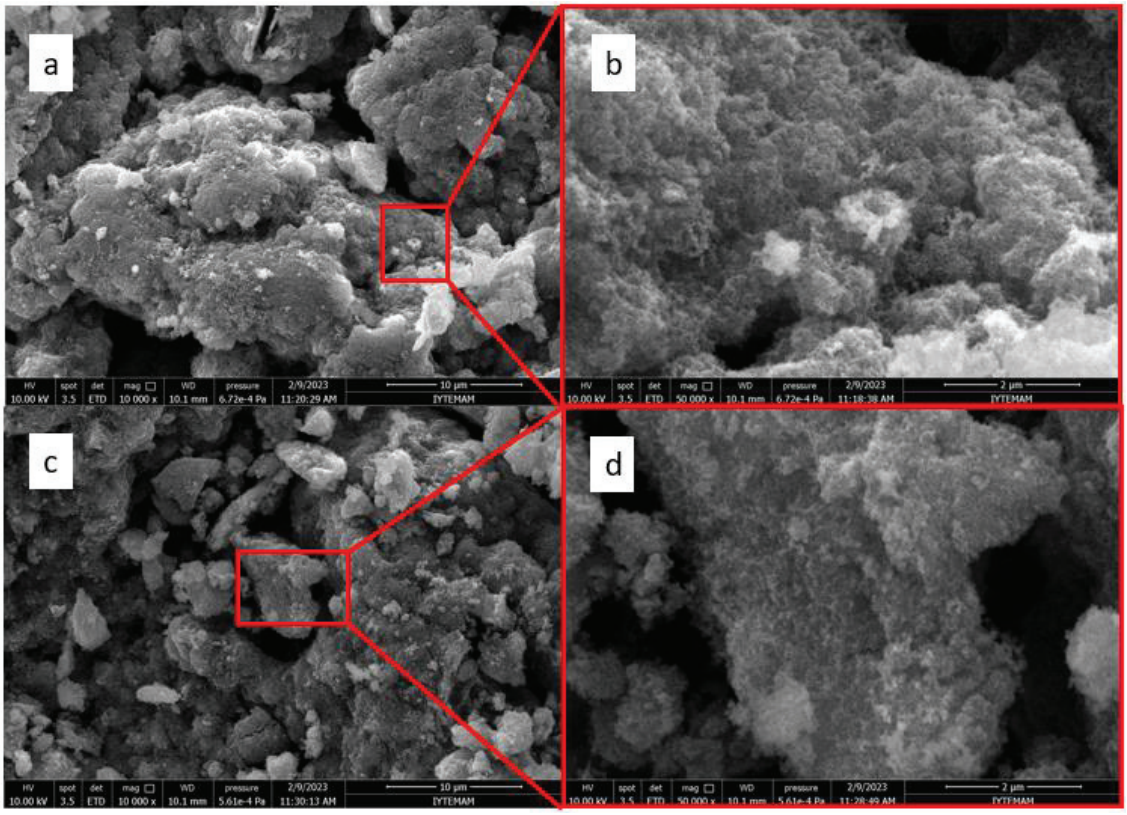

Figure 5.13. SEM images of (K)$Mn_xNi_yCo_zO_t$(1:0.5:0.5)-pH9.5@60°C (a) 10 000x, (b) 50 000x and (K)$Mn_xNi_yCo_zO_t$(1:1:1)-pH9.5@60°C (c) 10 000x, (d) 50 000x

Table 5.11. shows the EDX results of (S)$Mn_xNi_yCo_zO_t$(1:0.5:0.5)-pH9.5@60°C and (S)$Mn_xNi_yCo_zO_t$(1:1:1)-pH9.5@60°C sample. The purpose of the work is to produce a composite oxide consisting of manganese, nickel, and cobalt transition metals. The table shows that the mentioned transition metals are found in the sample (S)$Mn_xNi_yCo_zO_t$(1:0.5:0.5)-pH9.5@60°C. The purpose of the work is to produce a composite oxide consisting of manganese, nickel, and cobalt transition metals. The table shows that the mentioned transition metals are found in the sample (S)$Mn_xNi_yCo_zO_t$(1:1:1)-pH9.5@60°C. The atomic and weight percentages of Ni and Co are higher than the previous sample, which is expected due to the difference in the amount of precursor. When the concentration of nickel and cobalt solutions increased, the nickel and cobalt presence in the catalyst complex increased as expected.

Table 5.11. EDX results of (S)$Mn_xNi_yCo_zO_t$(1:0.5:0.5)-pH9.5@60°C sample

Element	(S)$Mn_xNi_yCo_zO_t$(1:0.5:0.5)		(S)$Mn_xNi_yCo_zO_t$(1:1:1)	
	Wt%	Atomic %	Wt%	Atomic %
O	28.81	58.49	27.74	57.52
Mn	56.00	33.12	43.08	26.01
Co	6.06	3.34	10.47	5.90
Ni	9.13	5.05	18.70	10.57
Total:	100.00	100.00	100.00	100.00

Table 5.12. shows the EDX results of (K)$Mn_xNi_yCo_zO_t$(1:0.5:0.5)-pH9.5@60°C and (K)$Mn_xNi_yCo_zO_t$(1:1:1)-pH9.5@60°C sample. The percentages shown in the table show that the study was concluded in accordance with the purpose. For the (K)$Mn_xNi_yCo_zO_t$(1:1:1)-pH9.5@60°C sample, percentages are more or less similar to each other with the previous sample. However, the Mn percentage is lower than the previous one. Therefore, the previous sample is more suitable for the purpose of the work. When the concentration of nickel and cobalt solutions increased, the nickel and cobalt presence in the catalyst complex increased a little less than expected.

Table 5.12. EDX results of (K)$Mn_xNi_yCo_zO_t$(1:0.5:0.5)-pH9.5@60°C and (K)$Mn_xNi_yCo_zO_t$(1:1:1)-pH9.5@60°C sample

Element	(K)$Mn_xNi_yCo_zO_t$(1:0.5:0.5)		(K)$Mn_xNi_yCo_zO_t$(1:1:1)	
	Wt%	Atomic%	Wt%	Atomic%
O	25.75	55.43	24.56	53.96
Mn	26.01	16.31	22.00	14.08
Co	18.80	10.99	20.12	12.01
Ni	29.44	17.27	33.32	19.95
Total:	100.00	100.00	100.00	100.00

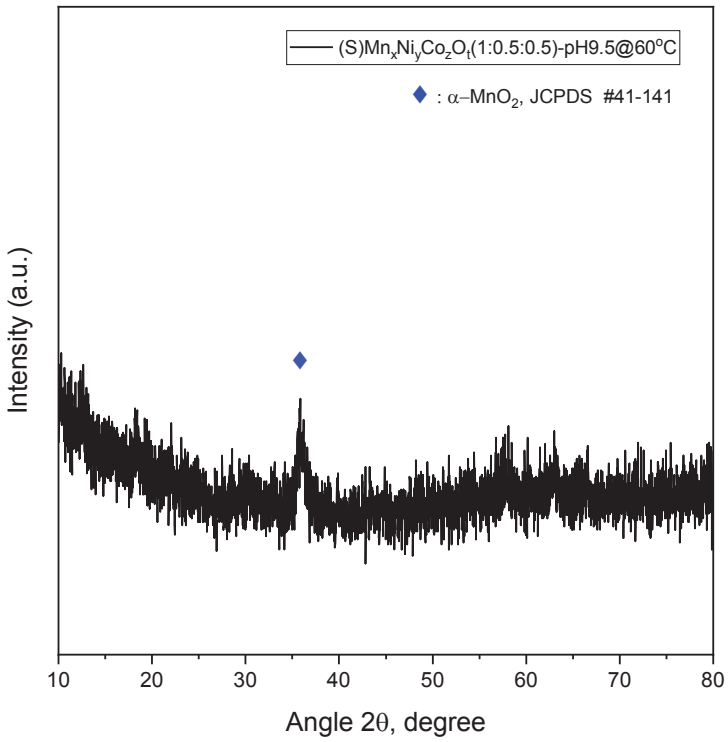

Figure 5.14. XRD graph of (S)$Mn_xNi_yCo_zO_t$(1:0.5:0.5)-pH9.5@60°C sample

Figure 5.14. shows the XRD graph of (S)$Mn_xNi_yCo_zO_t$(1:0.5:0.5)-pH9.5@60°C sample. There is one significant peak at 36° which is attributed to the α-MnO_2 compound (Feng, 2014). Other than that, Table 5.13. shows the chemical composition of a sample using the Rietveld Refinement Method. The dominant phase of the sample is α-MnO_2, with 70.6%. However, the CoO percentage is lower than aimed. When these two results are combined, it is seen that close results are obtained to the desired.

Table 5.13. Chemical composition of (S)$Mn_xNi_yCo_zO_t$(1:0.5:0.5)-pH9.5@60°C sample

Sample	α-MnO_2 (%)	NiO (%)	CoO (%)
1- (S)$Mn_xNi_yCo_zO_t$(1:0.5:0.5)-pH9.5@60°C	70.6	24.0	5.4

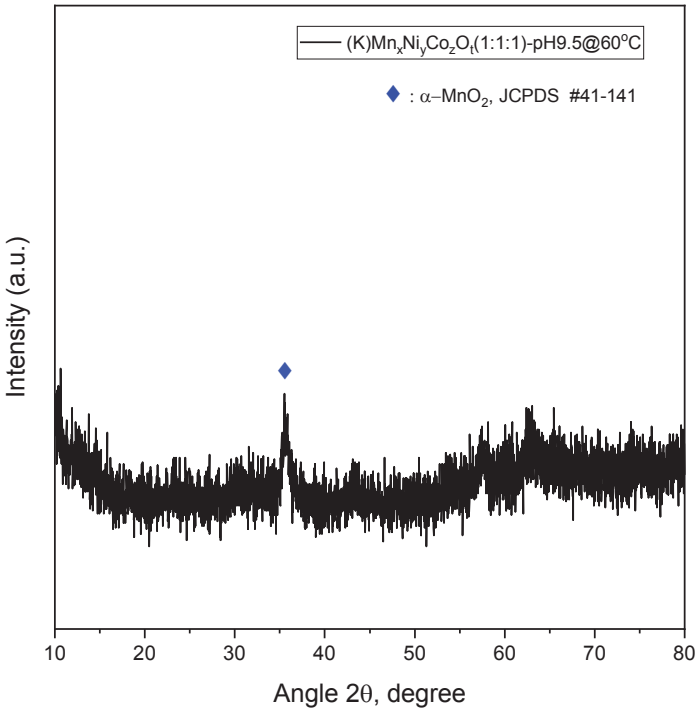

Figure 5.15. XRD graph of (S)$Mn_xNi_yCo_zO_t$(1:1:1)-pH9.5@60°C sample

Figure 5.15. shows the XRD graph of (S)$Mn_xNi_yCo_zO_t$(1:1:1)-pH9.5@60°C sample. There is one significant peak at 36° which is attributed to the α-MnO_2 compound (Feng, 2014). Other than that, Table 5.14. shows the chemical composition of a sample using the Rietveld Refinement Method. The dominant phase of the sample is α-MnO_2, with 47.7%. α-MnO_2 and NiO compositions are closer to each other than the previous sample. Also, CoO percentage is higher. This behavior is expected due to increased Nickel and Cobalt precursors during the reaction. When these two results are combined, the sample is preferable to the previous one.

Table 5.14. Chemical composition of (S)$Mn_xNi_yCo_zO_t$(1:1:1)-pH9.5@60°C sample

Sample	α-MnO_2 (%)	NiO (%)	CoO (%)
2- (S)$Mn_xNi_yCo_zO_t$(1:1:1)-pH9.5@60°C	47.6	37.8	14.6

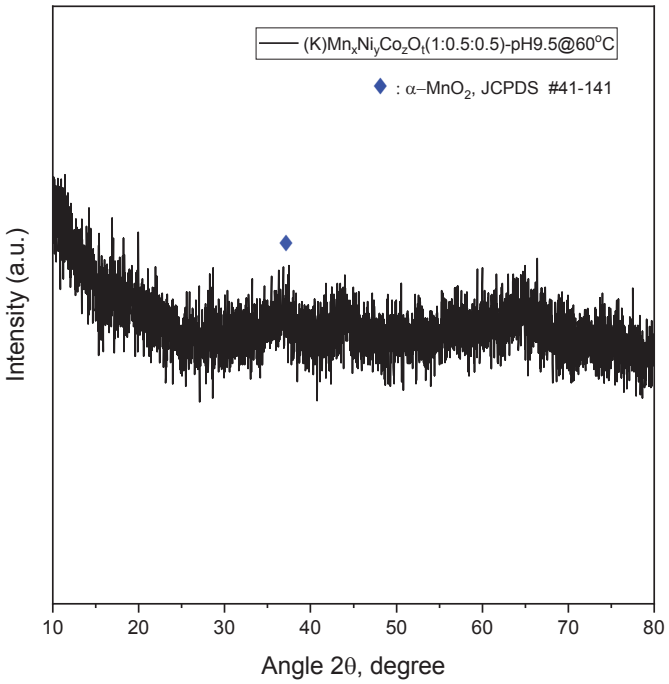

Figure 5.16. XRD graph of (K)$Mn_xNi_yCo_zO_t$(1:0.5:0.5)-pH9.5@60°C sample

Figure 5.16. shows the *XRD* graph of (K)$Mn_xNi_yCo_zO_t$(1:0.5:0.5)-pH9.5@60°C sample. There is one significant peak at 36° which is attributed to the α-MnO_2 compound (Feng, 2014). Other than that, Table 5.15. shows the chemical composition of a sample using the Rietveld Refinement Method. The dominant phase of the sample is α-MnO_2 and NiO. α-MnO_2 and NiO compositions are almost identical, with 44.8% and 44.7%. When these two results are combined, the sample is close enough to the purpose of the work.

Table 5.15. Chemical composition of (K)$Mn_xNi_yCo_zO_t$(1:0.5:0.5)-pH9.5@60°C sample

Sample	α-MnO_2 (%)	NiO (%)	CoO (%)
3- (K)$Mn_xNi_yCo_zO_t$(1:0.5:0.5)-pH9.5@60°C	44.8	44.7	10.5

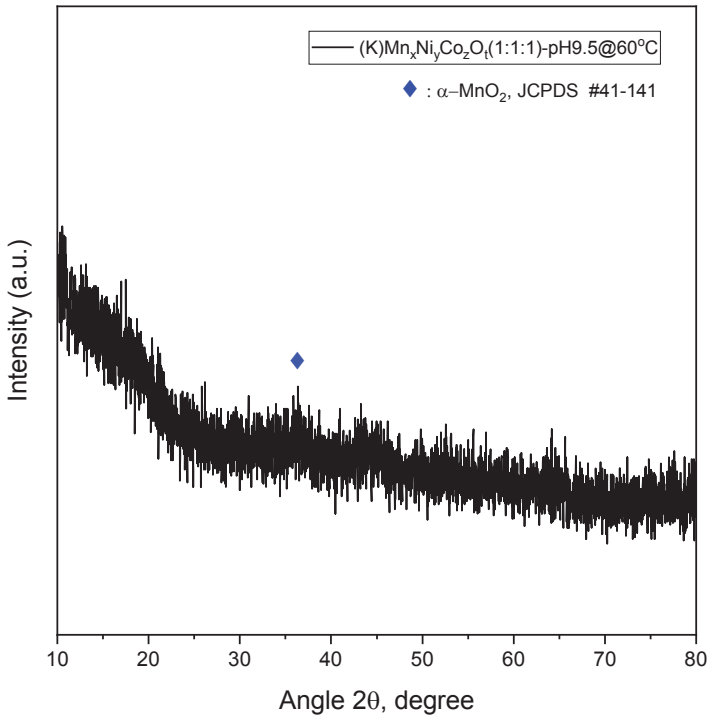

Figure 5.17. XRD graph of (K)$Mn_xNi_yCo_zO_t$(1:1:1)-pH9.5@60°C sample

Figure 5.17. shows the XRD graph of (K)$Mn_xNi_yCo_zO_t$(1:1:1)-pH9.5@60°C sample. There is one significant peak at 36° which is attributed to the α-MnO_2 compound (Feng, 2014). Other than that, Table 5.16. shows the chemical composition of a sample using the Rietveld Refinement Method. The dominant phase of the sample is α-MnO_2 with 50.3%. When this example is compared with the previous example, it is possible to determine which example will be better by looking at all other parameters.

Table 5.16. Chemical composition of (K)$Mn_xNi_yCo_zO_t$(1:1:1)-pH9.5@60°C sample

Sample	α-MnO_2 (%)	NiO (%)	CoO (%)
4- (K)$Mn_xNi_yCo_zO_t$(1:1:1)-pH9.5@60°C	50.3	37.8	11.9

Table 5.17. shows that the BET analysis results of the samples. The results obtained are expected when the results are compared in the literature (Mohd Yusof, 2018). There is a

significant difference between the samples with KMnO4(represented as “K”) and MnSO4.H2O (represented as “S”) as precursors almost 5-8 times superior in terms of BET surface area, which means more surface area for reactions to occur. Therefore, those are better candidates as electrocatalyzers. Also, the micropore area indicates the activity of a catalyst. As can be seen, the (K) samples show much better properties at that point as well. When we look at the comparison of those two samples using KMnO4 as a precursor, the precursor ratio of Mn:Ni: Co with 1:0.5:0.5 has a greater surface area. In addition to that, the micropore areas of both samples are similar to each other. Therefore, a higher surface area sample can be chosen as the candidate.

Table 5.17. BET Analysis results of samples

Sample	BET Surface Area, m^2g^{-1} (S_{BET})	Micropore Area, m^2g^{-1} (S_μ)	Total Pore Volume, cm^3g^{-1} (V_P)	Average Pore Diameter, nm ($d_{average}$)
(K)$Mn_xNi_yCo_zO_t$(1:1:1)-pH9.5@60°C	152.60	15.16	0.0069	6.31
(K)$Mn_xNi_yCo_zO_t$(1:0.5:0.5)-pH9.5@60°C	172.06	13.31	0.0056	7.80
(S)$Mn_xNi_yCo_zO_t$(1:1:1)-pH9.5@60°C	26.27	1.01	0.0003	8.65
(S)$Mn_xNi_yCo_zO_t$(1:0.5:0.5)-pH9.5@60°C	27.55	6.25	0.0032	7.67

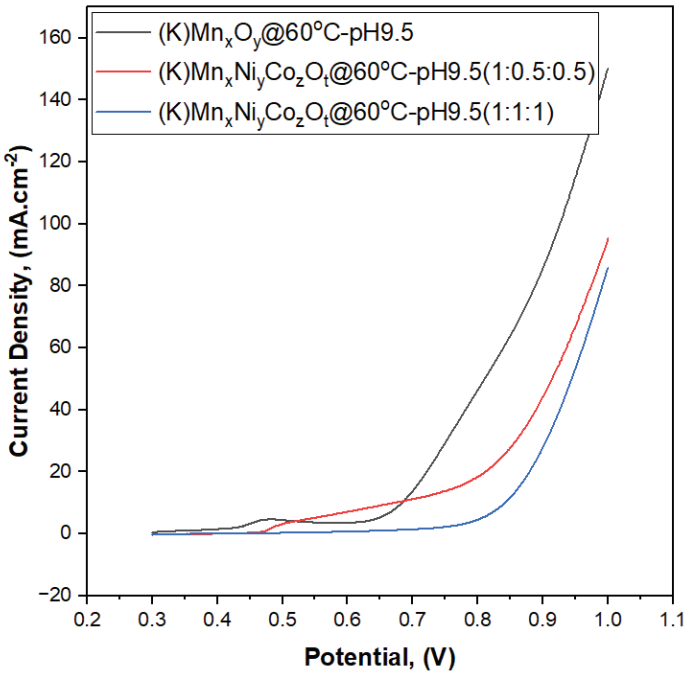

Figure 5.18. Linear Sweep Voltammogram of $(K)Mn_xO_y$-pH9.5@60°C, $(K)Mn_xNi_yCo_zO_t$(1:0.5:0.5)-pH9.5@60°C and $(K)Mn_xNi_yCo_zO_t$(1:1:1)-pH9.5@60°C

Figure 5.18. is the linear sweep voltammograms of the samples $(K)Mn_xO_y$-pH9.5@60°C, $(K)Mn_xNi_yCo_zO_t$(1:0.5:0.5)-pH9.5@60°C and $(K)Mn_xNi_yCo_zO_t$(1:1:1)-pH9.5@60°C. Linear sweep voltammetry tells that $(K)Mn_xNi_yCo_zO_t$(1:0.5:0.5)-pH9.5@60°C sample shows the best-desired overpotential for oxygen reduction reaction with 463mV and second best-desired overpotential for oxygen evolution reaction with 700mV. In the literature for oxygen reduction reactions, higher overpotential and oxygen evolution reactions with lower overpotential give greater catalytic activity, therefore, are more desirable than others (Cheng, 2013), (Ma, 2019). Overpotential values calculated from linear sweep voltammograms of catalysts individually can be seen in the appendix and listed in Table 5.18.

Table 5.18. Onset Overpotential Values of (K)Mn_xO_y-pH9.5@60°C, (K)$Mn_xNi_yCo_zO_t$(1:0.5:0.5)-pH9.5@60°C and (K)$Mn_xNi_yCo_zO_t$(1:1:1)-pH9.5@60°C

Catalyst	Onset Overpotential(mV), ORR	Onset Overpotential(mV), OER
(K)Mn_xO_y-pH9.5@60°C	412	560
(K)$Mn_xNi_yCo_zO_t$(1:0.5:0.5)-pH9.5@60°C	463	700
(K)$Mn_xNi_yCo_zO_t$(1:1:1)-pH9.5@60°C	400	770

Figure 5.19. shows the cycling voltammetry of the samples (K)Mn_xO_y-pH9.5@60°C, (K)$Mn_xNi_yCo_zO_t$(1:0.5:0.5)-pH9.5@60°C and (K)$Mn_xNi_yCo_zO_t$(1:1:1)-pH9.5@60°C. Electrocatalyst (K)Mn_xO_y-pH9.5@60°C has the highest current density with 151 mA.cm^{-2} and (K)$Mn_xNi_yCo_zO_t$(1:0.5:0.5)-pH9.5@60°C is the second best. Also the sample (K)$Mn_xNi_yCo_zO_t$(1:0.5:0.5)-pH9.5@60°C has the most desired phase composition with 44.8:44.7:10.5(α-MnO_2:NiO:CoO). Nickel amount is crucial in this perspective; when it is combined with manganese, nickel shows greater performance on both ORR and OER (Hao, 2017).

When compared with the current density of the commercial manganese dioxide reported in the previous section, the current density of the manganese oxide samples produced in the laboratory has increased more than five times.

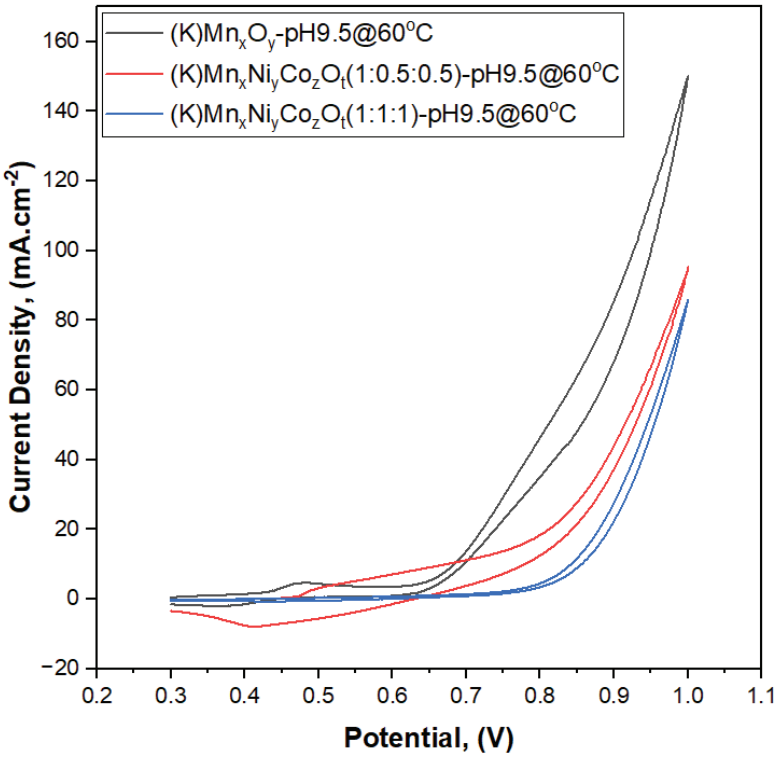

Figure 5.19. Cycling Voltammogram of $(K)Mn_xO_y$-pH9.5@60°C, $(K)Mn_xNi_yCo_zO_t$(1:0.5:0.5)-pH9.5@60°C and $(K)Mn_xNi_yCo_zO_t$(1:1:1)-pH9.5@60

Figure 5.20 shows the Tafel plots for the samples. Tafel slopes for both ORR and OER are calculated and listed in Table 5.19. The physical meaning of the Tafel slope indicates how much overpotential must be increased to increase the rate of a reaction. For this reason, a low Tafel slope is a desirable feature. The Tafel slopes of all catalysts are similar to each other except $(K)Mn_xNi_yCo_zO_t$(1:1:1)-pH9.5@60°C.

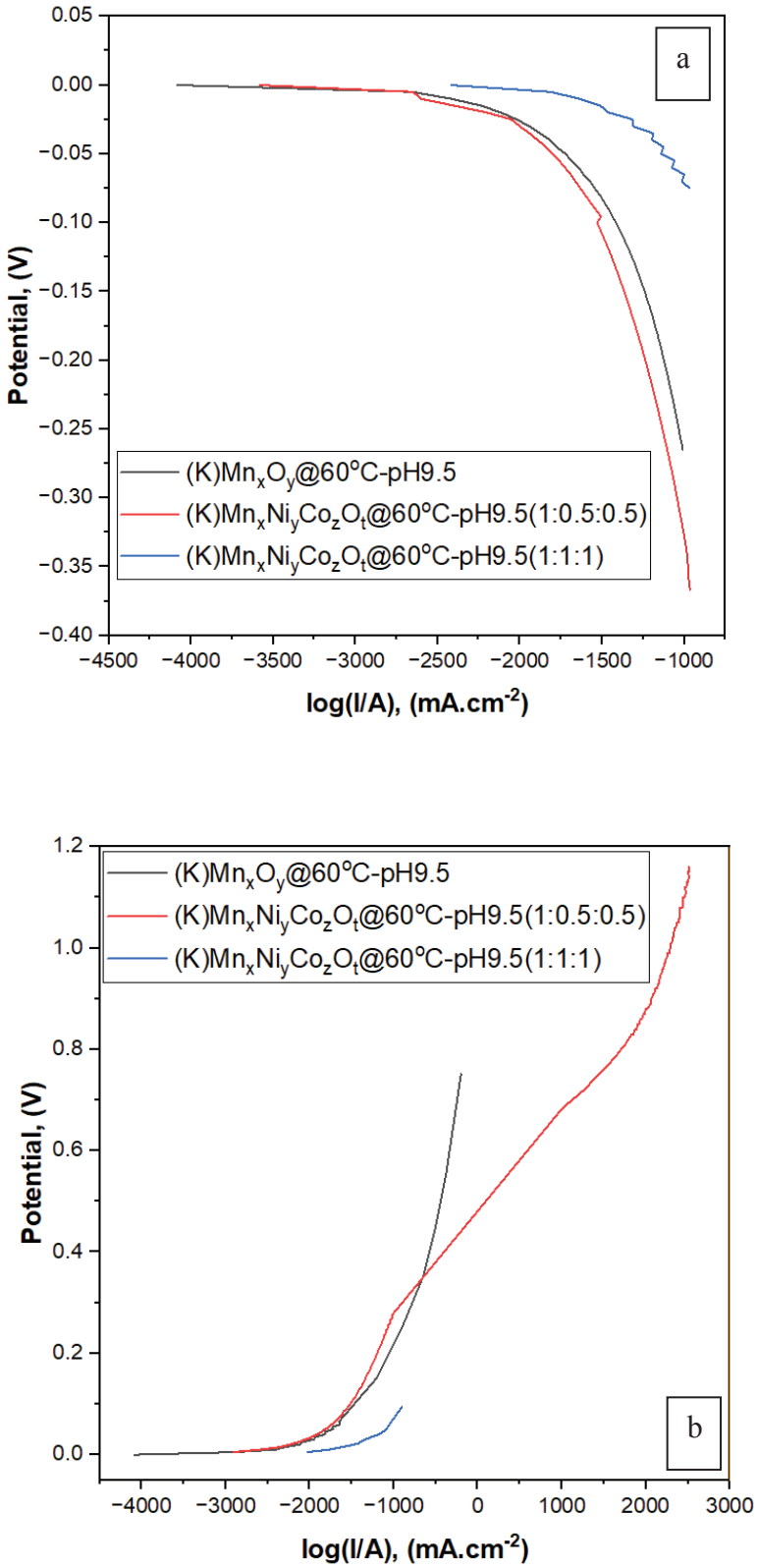

Figure 5.20. Tafel Plot of (K)Mn_xO_y-pH9.5@60°C, (K)$Mn_xNi_yCo_zO_t$(1:0.5:0.5)-pH9.5@60°C and (K)$Mn_xNi_yCo_zO_t$(1:1:1)-pH9.5@60°C for (a) ORR and (b) OER

Table 5.19. Tafel Slopes of Catalyst for ORR and OER

Catalyst	Tafel Slope (ORR), mV/dec	Tafel Slope (OER), mV/dec
(K)Mn_xO_y-pH9.5@60°C	22	20
(K)$Mn_xNi_yCo_zO_t$(1:0.5:0.5)-pH9.5@60°C	30	24
(K)$Mn_xNi_yCo_zO_t$(1:1:1)-pH9.5@60°C	59	72

Figure 5.23. shows the charge - discharge cycles of the samples (K)Mn_xO_y-pH9.5@60°C, (K)$Mn_xNi_yCo_zO_t$(1:0.5:0.5)-pH9.5@60°C and (K)$Mn_xNi_yCo_zO_t$(1:1:1)-pH9.5@60°C for 6.5 hours for each cycle consists of 20 minute discharge and 20 minute charge. The reason the charge-discharge cycle is determined as 6.5 hours is to test the short to long-term performance of the air electrode and to measure its ability to provide a stable current with 10 $mA.cm^{-2}$ to any external circuit during these periods. (K)$Mn_xNi_yCo_zO_t$(1:0.5:0.5)-pH9.5@60°C sample is showed more stable potential output for 6.5 hour than other samples. Of course, in the later stages of the study, it will be necessary to increase the number of cycles and thus increase the duration in order to better understand the charge-discharge stability. Additionally, the electrochemical analysis processes were carried out with a half-cell setup. When we consider half-cell and full-cell battery installations, in half-cell setups, results are obtained corresponding to the reference electrode, not the anode. For this reason, the performance of the electrode is close to ideal. However, in full-cell setups, the obtained results are in order to anode. Taking this into consideration in the future stages of the study, tests with full-cell setups should also be added to the study.

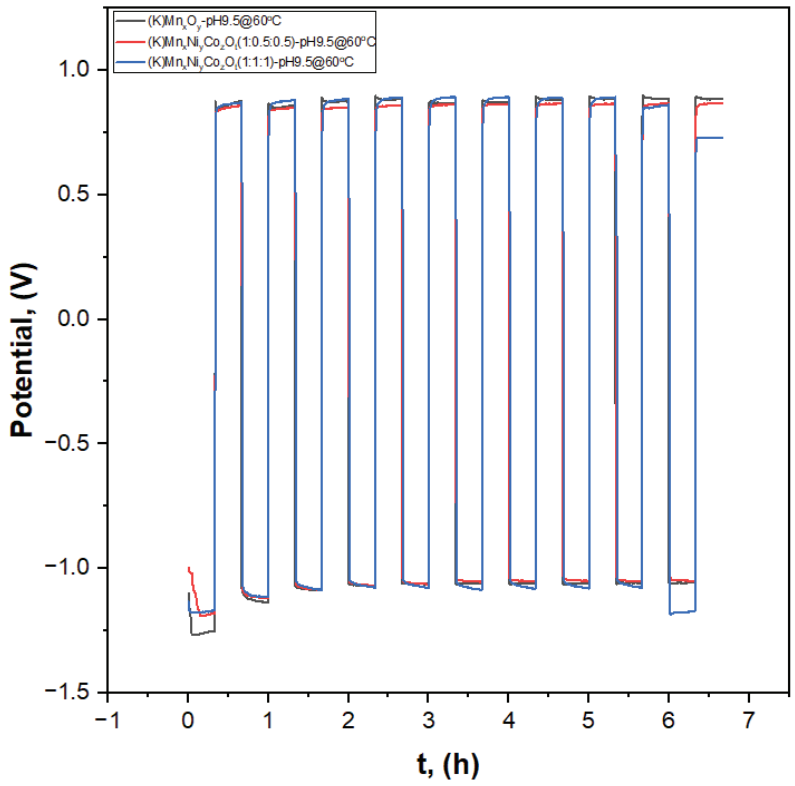

Figure 5.21. Charge-Discharge Curves of (K)Mn_xO_y-pH9.5@60°C, (K)$Mn_xNi_yCo_zO_t$(1:0.5:0.5)-pH9.5@60°C and (K)$Mn_xNi_yCo_zO_t$(1:1:1)-pH9.5@60°C

CHAPTER 6

CONCLUSION

This thesis has been carried out with the aim of synthesizing a catalyst for the catalyst layer in air electrode of rechargeable zinc-air batteries within the scope of the M-Era.NET "AMAZE" 2020 Project. The main purpose of AMAZE 2020 Project is to produce fully functioning zinc-air battery with three different contributors. This project focuses on the air electrode of the mentioned zinc-air battery.

First of all, the preliminary research conducted to select the catalyst material. Due to their desired features mentioned in Chapter 1 and 2, transition metal oxides are good candidates for the job instead of widely using noble metals. In the first evaluation manganese oxides selected. Synthesize method was chosen as co-precipitation method due its scalability and ease of controllability of parameters. Different parameters were investigated such as precursor amount, pH, temperature and different precursors in the beginning two different precursors which are $KMnO_4$ and $MnSO_4.H_2O$ were discussed to synthesize manganese oxide particles. After various evaluations, KMnO4 catalysts always outperform the MnSO4.H2O catalyst in all desired features. Therefore, $KMnO_4$ was selected as a definite precursor. Then, the optimum parameter conditions were determined as pH 9.5 and temperature 60°C after a series of methodological attempts within the scope of various physical characterization features such as surface area, surface morphology, and crystal structure. (K)Mn_xO_y-pH9.5@60°C has the highest surface area with 85.68 m^2g^{-1} and also has the most desired phase of the manganese oxide for electrochemical reactions, α-MnO_2. In addition, the electrochemical characterization results are matching with the physical characterization results. (K)Mn_xO_y-pH9.5@60°C has the desired onset overpotentials for ORR and OER with 650mV and 271mV. Also, the catalyst has the highest current density among the others, with 10.5 $mA.cm^{-2}$. In addition to that, the Tafel slope of (K)Mn_xO_y-pH9.5@60°C showed that it is the second best to the commercial MnO_2. Therefore, the catalyst is suitable for the job.

However, in addition to the work done so far, some improvements were considered due to the potential to improve the properties sought in the produced

catalysts. The idea was to produce a more complex bifunctional metal oxide based on manganese oxide that works for both ORR and OER. Nickel and cobalt are the first transition metals that come to mind with co-operating to manganese. Afterwards, the amounts of nickel and cobalt to be added to manganese were determined by volume. Two different catalysts were synthesized with Mn:Ni:Co precursor solution ratios of 1:1:1 and 1:0.5:0.5 by volume. Then synthesis studies were also carried out for $MnSO_4.H_2O$, which was also used initially. However, the catalysts those used $MnSO_4.H_2O$ as precursor showed inefficient results in terms of features like previous catalysts. Therefore, there were three final catalysts to evaluate the best among them. So, the physical and electrochemical characterizations were conducted among the remained catalysts again. The catalyst (K)$Mn_xNi_yCo_zO_t$(1:0.5:0.5)-pH9.5@60°C were outperformed other catalysts. (K)$Mn_xNi_yCo_zO_t$(1:0.5:0.5)-pH9.5@60°C has the highest surface area with 172.06 m^2g^{-1}. It also has the desired chemical composition of Mn:Ni:Co with 45:44:11. In addition to that the catalyst has the best desired overpotential for oxygen reduction reaction with 463mV and second best desired overpotential for oxygen evolution reaction with 700mV. (K)$Mn_xNi_yCo_zO_t$(1:0.5:0.5)-pH9.5@60°C has the second-best current density with 96 $mA.cm^{-2}$. However, when it comes to ORR and OER, it shows the best performance. However, when looking at the Tafel slopes, there was not much difference between the catalysts. Finally, charge-discharge tests showed that all catalysts sustained their electrochemical durability.

In conclusion, the findings obtained as a result of the studies indicate that the catalyst produced might be a step towards commercialization. Of course, the necessary feasibility studies should be continued while commercialization steps are taken. As a result, since the study is at the laboratory level, it should be subjected to a scale-up process and re-evaluated. At this point, the suitability of the chosen production method(co-precipitation) for scale-up provides a comfortable basis for future studies.

REFERENCES

Ahmed, K. A. M., & Huang, K. (2019). Formation of Mn_3O_4 nanobelts through the solvothermal process and their photocatalytic property. *Arabian Journal of Chemistry*, *12*(3), 429–439. https://doi.org/10.1016/j.arabjc.2014.08.014

Bai, F., He, Y., Xu, L., Wang, Y., Wang, Y., Hao, Z., & Li, F. (2022). Improved ORR/OER bifunctional catalytic performance of amorphous manganese oxides prepared by photochemical metal–organic deposition. RSC Advances, 12(4), 2408–2415. https://doi.org/10.1039/d1ra08618a

Bag S, Roy K, Gopinath CS, Raj CR (2014) Facile single-step synthesis of nitrogen-doped reduced graphene oxide-$Mn_{(3)}O_{(4)}$ hybrid functional material for the electrocatalytic reduction of oxygen. ACS Appl Mater Interfaces 6(4):2692–2699

Bard, A. J., & Fox, M. A. (1995). Artificial photosynthesis: solar splitting of water to hydrogen and oxygen. Accounts of Chemical Research, 28(3), 141-145.

Bekisch, A., Skadell, K., Poppitz, D., Schulz, M., Weidl, R., & Stelter, M. (2020). Hydrophobic, Carbon Free Gas Diffusion Electrode for Alkaline Applications. Journal of The Electrochemical Society, 167(14), 144502. https://doi.org/10.1149/1945-7111/abbdd4

Burke, A. (2008). R&D considerations for the performance and application of rechargeable lithium batteries. Progress in Solid State Chemistry, 36(1-2), 133-144. doi:10.1016/j.progsolidstchem.2008.06.001

Brousse, T., Toupin, M., Dugas, R., Athouë L, L., Crosnier, O., & BéLanger, D. (2006). Crystalline MnO_2 as Possible Alternatives to Amorphous Compounds in Electrochemical Supercapacitors. Journal of The Electrochemical Society, 153(12), A2171. https://doi.org/10.1149/1.2352197

Bruce, P. G., Freunberger, S. A., Hardwick, L. J., & Tarascon, J. M. (2012). Li–O_2 and Li–S batteries with high energy storage. Nature materials, 11(1), 19-29.

Cao, W., Zhang, J., & Li, H. (2020). Batteries with high theoretical energy densities. Energy Storage Materials, 26, 46–55. https://doi.org/10.1016/j.ensm.2019.12.024

Cadu, S., *Zinc-air batteries | IoLiTec*. (2018). Zinc - Air Batteries. Retrieved February 16, 2022, from https://iolitec.de/en/node/648

Chen, C., Kang, B., & Chung, C. H. (2017). Recent advances in Li-air batteries. Advanced Energy Materials, 7(13), 1602466.

Chen, Y., Freunberger, S. A., Peng, Z., Fontaine, O., & Bruce, P. G. (2015). Charging a Li–O_2 battery using a redox mediator. Nature Chemistry, 7(4), 366-371.s

Chen, P., Zhang, K., Tang, D., Li, W., Meng, F., Huang, Q., & Liu, J. (2020). Recent progress in electrolytes for ZN–Air batteries. Frontiers in Chemistry, 8. https://doi.org/10.3389/fchem.2020.00372

Chen, W., Xiang, W., Li, W., Zhang, H., Du, F., Zhao, T., Xiao, Q., Li, X., & Luo, W. (2023a). An ultrathin defect-rich nickel–cobalt oxide nanosheet array for enhanced bifunctional oxygen electrocatalysis. Inorganic Chemistry Frontiers, 10(4), 1127– 1135. https://doi.org/10.1039/d2qi02487j

Cheng, Y., Zhang, R., Zhao, Y., & Liu, G. (2017). A review on the key issues for lithium-ion battery management in electric vehicles. Journal of Power Sources, 226, 272-288.

Cherian, E., Rajan, A., Baskar, G. (2016). Synthesis of manganese dioxide nanoparticles using co-precipitation method and its antimicrobial activity. Internation Journal of Modern Science and Technology, 1(1), 17-22.

Crompton, T. R. (2000). *Battery Reference Book* (3rd ed.). Newnes.

Dunn, B., Kamath, H., & Tarascon, J.-M. (2011). Electrical Energy Storage for the Grid: A Battery of Choices. Science, 334(6058), 928-935.

International Energy Agency (IEA). (2020). Global Energy Review 2020. Retrieved from https://www.iea.org/reports/global-energy-review-2020

Dai, Y., Yu, J., Cheng, C. H., Tan, P., & Ni, M. (2020). Mini-review of perovskite oxides as oxygen electrocatalysts for rechargeable zinc–air batteries. Chemical Engineering Journal, 397, 125516. https://doi.org/10.1016/j.cej.2020.125516

Deng, W., Li, G., Wu, T., Li, H., Wu, J., Liu, J., Zheng, H., Li, X., Yang, Y., Jing, M., Wang, Y., & Wang, X. (2022). Heteroatom functionalized double-layer carbon nanocages as highly efficient oxygen electrocatalyst for Zn-Air batteries. Carbon, 186, 589–598. https://doi.org/10.1016/j.carbon.2021.10.057

Ezeigwe, E. R., Li, D., Wang, J., Wang, L., Wang, Y., & Zhang, J. (2020). MOF-deviated zinc-nickel–cobalt ZIF-67 electrode material for high-performance symmetrical coin-shaped supercapacitors. Journal of Colloid and Interface Science, 574, 140–151. https://doi.org/10.1016/j.jcis.2020.04.025

Feng, L., (2014). MnO_2 prepared by hydrothermal method and electrochemical performance as anode for lithium-ion battery. *Nanoscale Research Letters*, *9*(1). https://doi.org/10.1186/1556-276-9-290

Fu, J., Cano, Z. P., Park, M. G., Yu, A., Fowler, M., & Chen, Z. (2016). Electrically rechargeable Zinc-Air batteries: Progress, challenges, and perspectives. Advanced Materials, 29(7). https://doi.org/10.1002/adma.201604685

Fujimoto, K., Ueda, Y., Inohara, D., Fujii, Y., & Nakayama, M. (2020). Cobalt-doped electrolytic manganese dioxide as an efficient bifunctional catalyst for oxygen evolution/reduction reactions. Electrochimica Acta, 354, 136592. https://doi.org/10.1016/j.electacta.2020.136592

García, G. R., Ventosa, E., & Schuhmann, W. (2017). Complete prevention of dendrite formation in ZN metal anodes by means of pulsed charging protocols. ACS Applied Materials & Interfaces, 9(22), 18691–18698. https://doi.org/10.1021/acsami.7b01705

Guo, Z., Zhou, H., & Li, L. (2017). Recent progress in zinc-air batteries. Chemical Society Reviews, 46(20), 5767-5801.

Gonçalves, G., Boinamo, R. P., & Rocha, C. G. (2020). Review of Zinc-Air Batteries for Automotive Application. Journal of Energy Storage, 32, 101651.

Han, L., Yu, X., & Lou, X. W. D. (2016). Formation of Prussian-Blue-Analog Nanocages via a Direct Etching Method and their Conversion into Ni-Co-Mixed Oxide for Enhanced Oxygen Evolution. Advanced Materials, 28(23), 4601–4605. https://doi.org/10.1002/adma.201506315

Hannah Ritchie, Max Roser and Pablo Rosado (2022) - "Energy". Published online at OurWorldInData.org. Retrieved from: 'https://ourworldindata.org/energy'

Hao, Y., Xu, Y., Liu, J., & Sun, X. (2017b). Nickel–cobalt oxides supported on Co/N decorated graphene as an excellent bifunctional oxygen catalyst. Journal of Materials Chemistry. A, Materials for Energy and Sustainability, 5(11), 5594–5600. https://doi.org/10.1039/c7ta00299h

Hernandez-Aldave, S., & Andreoli, E. (2020). Fundamentals of Gas Diffusion Electrodes and Electrolysers for carbon dioxide utilisation: Challenges and opportunities. Catalysts, 10(6), 713. https://doi.org/10.3390/catal10060713

Hosseini, S., Lao-Atiman, W., Han, S. J., Arpornwichanop, A., Yonezawa, T., &

Kheawhom, S. (2018). Discharge performance of Zinc-Air flow batteries under the effects of sodium dodecyl sulfate and pluronic F-127. Scientific Reports, 8(1). https://doi.org/10.1038/s41598-018-32806-3

Ji, X., et al. (2011). A Highly Ordered Nanostructured Carbon–Sulfur Cathode for Lithium–Sulfur Batteries. Nature Materials, 8(6), 500-506.

Jiao, Y., Zheng, Y., Jaroniec, M., & Qiao, S. Z. (2014). Origin of the Electrocatalytic Oxygen Reduction Activity of Graphene-Based Catalysts: A Roadmap to Achieve the Best Performance. Journal of the American Chemical Society, 136(11), 4394– 4403. https://doi.org/10.1021/ja500432

Julien, C., Mauger, A., Vijh, A., & Zaghib, K. (2015). *Lithium Batteries: Science and Technology* (1st ed. 2016 ed.). Springer.

Kanha, P., (2017). Effect of stirring time on morphology and crystalline features of MnO_2 nanoparticles synthesized by co-precipitation method. *Inorganic and Nano-Metal Chemistry*, *47*(8), 1129–1133. https://doi.org/10.1080/24701556.2017.1284100

King'ondu, C. K., Opembe, N. N., Genuino, H. C., Garces, H. F., Njagi, E. C., Iyer, A., Huang, H., Dharmarathna, S., & Suib, S. L. (2011). Nonthermal Synthesis of Three-Dimensional Metal Oxide Structures under Continuous-Flow Conditions and Their Catalytic Applications. The Journal of Physical Chemistry C, 115(47), 23273–23282. https://doi.org/10.1021/jp206942u

Kordesch, K., & Simader, G. (1980). Primary Zinc–Air Cells. Journal of Power Sources, 5(2), 97-105.

Lee, J. S., Tai Kim, S., Cao, R., Choi, N. S., Liu, M., Lee, K. T., & Cho, J. (2010). Metal-Air Batteries with High Energy Density: Li-Air versus Zn-Air. Advanced Energy Materials, 1(1), 34–50. https://doi.org/10.1002/aenm.201000010

Lee, D. U., & Park, M. S. (2017). Scalable and sustainable approach toward highly active and robust fuel cell catalysts with ultralow loading. Advanced Materials, 29(8), 1604167.

Li, F., Wu, Z., Zhang, W., & Wang, W. (2016). High-energy-density non-aqueous zinc-air batteries with nano-structured bismuth-modified carbon paper cathode. Nano Energy, 19, 282-291.

Li, X., Pletcher, D., Russell, A. E., Walsh, F. C., Wills, R., Gorman, S. F., Price, S. W. T., & Thompson, S. (2013). A novel bifunctional oxygen GDE for alkaline secondary batteries. Electrochemistry Communications, 34, 228–230. https://doi.org/10.1016/j.elecom.2013.06.020

Li, Y., & Lu, J. (2017). Metal–Air Batteries: Will They Be the Future Electrochemical Energy Storage Device of Choice? ACS Energy Letters, 2(6), 1370–1377. https://doi.org/10.1021/acsenergylett.7b00119

Li, J., Zhao, T. S., & Chen, Y. (2013). Zinc-air batteries: A mini review. Journal of Power Sources, 229, 158-167.

Li, M., Lu, J., Chen, Z., & Amine, K. (2013). 15-Advanced materials for advanced zinc-air batteries. In Advanced Materials for Sustainable Developments (pp. 407-432).

Li, Y., Gong, M., Liang, Y., Feng, J., Kim, J., Wang, H., Hong, G., Zhang, B., & Dai, H. (2013). Advanced zinc-air batteries based on high-performance hybrid electrocatalysts. Nature Communications, 4(1). https://doi.org/10.1038/ncomms2812

Li, Y., & Lü, J. (2017). Metal–Air batteries: Will they be the future electrochemical energy storage device of choice? ACS Energy Letters, 2(6), 1370–1377. https://doi.org/10.1021/acsenergylett.7b00119

Liang, X., Rui, K., Xing, L., Wang, G., & Zhuang, L. (2017). Zinc-Air Batteries: Challenges and Opportunities. Electrochimica Acta, 235, 146-156.

Liang, Z., Lu, J., & Luo, J. (2017). Metal-Air Batteries: Will They Be the Future Electrochemical Energy Storage Device of Choice? ACS Energy Letters, 2(6), 1370-1377.

Liu, X., Chang, Z., Luo, L., Xu, T., Lei, X., Liu, J., & Sun, X. (2014). Hierarchical $Zn_xCo_{3-x}O_4$ Nanoarrays with High Activity for Electrocatalytic Oxygen Evolution. Chemistry of Materials, 26(5), 1889–1895. https://doi.org/10.1021/cm4040903

Liu, S., Han, W., Cui, B., Liu, X., Sun, H., Zhang, J., Lefler, M., & Licht, S. (2018). Rechargeable Zinc Air Batteries and Highly Improved Performance through Potassium Hydroxide Addition to the Molten Carbonate Eutectic Electrolyte. Journal of the Electrochemical Society, 165(2), A149–A154. https://doi.org/10.1149/2.0491802jes

Lu, Y., Goodenough, J. B., & Kim, Y. (2017). Aqueous solution growth of monodisperse α-MnO_2 nanorods as high performance cathodes for sodium ion batteries. Advanced Energy Materials, 7(7), 1601993.

Lu, B., Cao, D., Wang, P., & Gao, Y. (2011). Oxygen evolution reaction on Ni-substituted Co_3O_4 nanowire array electrodes. International Journal of Hydrogen Energy, 36(1), 72–78. https://doi.org/10.1016/j.ijhydene.2010.09.056

Loh, A., Xu, K., Li, X., & Wang, B. (2017). Influence of synthesis parameters on amorphous manganese dioxide catalyst electrocatalytic performance. Electrochimica Acta, 245, 615–624. https://doi.org/10.1016/j.electacta.2017.05.188

Ma, R., Lin, G., Zhou, Y., Liu, Q., Zhang, T., Shan, G., Yang, M., & Wang, J. (2019b). A review of oxygen reduction mechanisms for metal-free carbon-based electrocatalysts. Npj Computational Materials, 5(1). https://doi.org/10.1038/s41524- 019-0210-3

Mainar, A. R., Iruin, E., Colmenares, L. C., Kvasha, A., de Meatza, I., Bengoechea, M., Leonet, O., Boyano, I., Zhang, Z., & Blazquez, J. A. (2018). An overview of progress in electrolytes for secondary zinc-air batteries and other storage systems based on zinc. Journal of Energy Storage, 15, 304–328. https://doi.org/10.1016/j.est.2017.12.004

Mainar, A. R., Colmenares, L. C., Leonet, O., Alcaide, F., Iruin, J. J., Weinberger, S., Hacker, V., Iruin, E., Urdanpilleta, I., & Blázquez, J. A. (2016b). Manganese oxide catalysts for secondary zinc air batteries: from electrocatalytic activity to bifunctional air electrode performance. Electrochimica Acta, 217, 80–91. https://doi.org/10.1016/j.electacta.2016.09.052

Martindale, B., & Reisner, E. (2015). Bi-Functional Iron-Only Electrodes for Efficient Water Splitting with Enhanced Stability through In Situ Electrochemical Regeneration. Advanced Energy Materials, 6(6). https://doi.org/10.1002/aenm.201502095

Min, Y. J., Oh, S. J., Kim, M. S., Choi, J. H., & Eom, S. (2018). Effect of carbon properties on the electrochemical performance of carbon-based air electrodes for rechargeable zinc–air batteries. *Journal of Applied Electrochemistry*, *48*(4), 405–413. https://doi.org/10.1007/s10800-018-1173-7

Miyazaki, K., Lee, Y. S., Fukutsuka, T., & Abe, T. (2012). Suppression of Dendrite Formation of Zinc Electrodes by the Modification of Anion-Exchange Ionomer. Electrochemistry, 80(10), 725–727. https://doi.org/10.5796/electrochemistry.80.725

Mladenova, E., Slavova, M., Mihaylova-Dimitrova, E., Burdin, B., Abrashev, B., Krapchanska, M., Raikova, G., & Vladikova, D. (2021). Monolithic carbon-free gas diffusion electrodes for secondary metal-air batteries. Journal of Electroanalytical Chemistry, 887, 115112. https://doi.org/10.1016/j.jelechem.2021.115112

Mohd Yusof, S. N. N., Mohd Zain, N. K., Misnon, I. I., & Jose, R. (2018). Electrochemical Evaluation of Fluorinated MnO2 for Supercapacitor Application. MATEC Web of Conferences, 150, 02006. https://doi.org/10.1051/matecconf/201815002006

Munaiah, Y. (2013). Facile synthesis of hollow sphere amorphous MnO2: the formation mechanism, morphology and effect of a bivalent cation-containing electrolyte on its supercapacitive behavior. *Journal of Materials Chemistry A*, *1*(13), 4300. https://doi.org/10.1039/c3ta01089a

Nazri, G. A., & Tan, T. (1994). Metal-air batteries: Fundamentals and applications. Electrochimica Acta, 39(11-12), 1883-1900.

Ng, J. W. D., Tang, M. H., & Jaramillo, T. F. (2014). A carbon-free, precious-metal-free, high-performance O_2 electrode for regenerative fuel cells and metal–air batteries. Energy and Environmental Science, 7(6), 2017. https://doi.org/10.1039/c3ee44059a

Olabi, A. G., Sayed, E. T., Wilberforce, T., Jamal, A., Alami, A. H., Elsaid, K., Rahman, S. M. A., Shah, S. K., & Abdelkareem, M. A. (2021). Metal-Air Batteries—A Review. Energies, 14(21), 7373. https://doi.org/10.3390/en14217373

Park, M., Zhang, X., Chung, M., Less, G. B., & Sastry, A. M. (2010). A review of conduction phenomena in Li-ion batteries. Journal of Power Sources, 195(24), 7904–7929. https://doi.org/10.1016/j.jpowsour.2010.06.060

Peng, S. (2023). Zinc-Air batteries: Fundamentals, Key Materials and Application. Springer.

Pei, P., Wang, K., & Ma, Z. (2014). Technologies for extending zinc–air battery's cyclelife: A review. *Applied Energy*, *128*, 315–324. https://doi.org/10.1016/j.apenergy.2014.04.095

Qi, J., Chen, M., Zhang, W., & Cao, R. (2019). Hierarchical-dimensional Material: A $Co(OH)_2$ Superstructure with Hybrid Dimensions for Enhanced Water Oxidation. ChemCatChem, 11(24), 5969–5975. https://doi.org/10.1002/cctc.201900697

Rout, S., Nayak, A. K., Varanasi, J. L., Pradhan, D., & Das, D. (2018). Enhanced energy recovery by manganese oxide/reduced graphene oxide nanocomposite as an air-cathode electrode in the single-chambered microbial fuel cell. Journal of Electroanalytical Chemistry, 815, 1–7. https://doi.org/10.1016/j.jelechem.2018.03.002

Sagadevan, S. (2015). Investigations on Synthesis, Structural, Morphological and Dielectric Properties of Manganese Oxides Nanoparticles. Journal of Material Science & Engineering, 04(03). https://doi.org/10.4172/2169-0022.1000172

Scrosati, B., & Garche, J. (2010). Lithium Batteries: Status, Prospects and Future. Journal of Power Sources, 195(9), 2419-2430.

Singh, R. (2018). Review on high energy density metal-air batteries. Journal of Power Sources, 382, 176-197.

Smolinka, T., & Garche, J. (2021). Electrochemical Power Sources: fundamentals, systems, and applications: Hydrogen Production by Water Electrolysis. Elsevier.

Song, J., Xu, T., Gordin, M. L. et al. (2015). Nitrogen-doped graphene nanosheets as cathode materials with excellent electrocatalytic performance for high-performance rechargeable Li-O_2 batteries. Chemistry of Materials, 27(11), 4123-4132. doi: 10.1021/acs.chemmater.5b01389

Sun, Y., Zhang, X., Luo, M., Chen, X., Wang, L., Li, Y., Li, M., Qin, Y., Li, C., Xu, N., Lu, G., Gao, P., & Guo, S. (2018). Ultrathin PtPd-Based Nanorings with Abundant Step Atoms Enhance Oxygen Catalysis. Advanced Materials, 30(38), 1802136. https://doi.org/10.1002/adma.201802136

Tao, F., Liu, Y., Ren, X., Wang, J., Zhou, Y., Miao, Y., Ren, F., Wei, S., & Ma, J. (2022). Different surface modification methods and coating materials of zinc metal anode. Journal of Energy Chemistry, 66, 397–412. https://doi.org/10.1016/j.jechem.2021.08.022

Tang, W., (2014). Sol–gel process for the synthesis of ultrafine MnO_2 nanowires and nanorods. *Materials Letters*, *132*, 317–321. https://doi.org/10.1016/j.matlet.2014.05.211

Trasatti, S. (1991). Physical electrochemistry of ceramic oxides. *Electrochimica Acta*, *36*(2), 225–241. https://doi.org/10.1016/0013-4686(91)85244-2

Torabi, F., & Ahmadi, P. (2020). Battery technologies. In Elsevier eBooks (pp. 1–54). https://doi.org/10.1016/b978-0-12-816212-5.00005-2

Wang, J., Kong, F., Wang, Z., Ren, M., Qiao, C., Liu, W., Yao, J., Zhang, C., & Zhao, H. (2023). Dendrite-Free zinc deposition induced by an artificial layer of strontium titanate for stable zinc metal anode. Journal of the Electrochemical Society. https://doi.org/10.1149/1945-7111/acdd9e

Wang, H.F., Tang, C., and Zhang, Q. (2018). A review of precious-metal-free bifunctional oxygen electrocatalysts: rational design and applications in Zn-air batteries. Adv. Funct. Mater. 28, 1803329.

Wang, H., S. Xu, C. Tsai, Y. Li, C. Liu, J. Zhao, Y. Liu, H. Yuan, F. Abild-Pedersen, F.B. Prinz, J.K. Norskov, Y. Cui, Direct and continuous strain control of catalysts with tunable battery electrode materials, Science 354 (2016) 1031–1036.

Wang, P., (2019). Construction of a Janus MnO_2-NiFe Electrode via Selective Electrodeposition Strategy as a High-Performance Bifunctional Electrocatalyst for Rechargeable Zinc–Air Batteries. *ACS Applied Materials & Interfaces*, *11*(41), 37701–37707. https://doi.org/10.1021/acsami.9b12232

Wei, Z., Lu, Z., Yuan, J., & Yang, S. (2018). Nanostructured electrocatalysts for PEM fuel cells and alkaline water electrolyzer. Chemical Society Reviews, 47(21), 7712-7737.

Whittingham, M. S. (1977). Advances in Zinc-Air Batteries. Advanced Energy Conversion, 17(1), 133-150.

Worku, A. K., Ayele, D. W., Habtu, N. G., Teshager, M. A., & Workineh, Z. G. (2021). Recent progress in MnO_2-based oxygen electrocatalysts for rechargeable zinc-air batteries. Materials Today Sustainability, 13, 100072. https://doi.org/10.1016/j.mtsust.2021.100072

Wu, M., Zhang, G., Wu, M., Prakash, J., & Sun, S. (2019). Rational design of multifunctional air electrodes for rechargeable Zn–Air batteries: Recent progress and future perspectives. Energy Storage Materials, 21, 253–286. https://doi.org/10.1016/j.ensm.2019.05.018

Wu, X., Ji, X., Sun, Z., & Jin, J. (2018). Zinc-Air Batteries: A Review of the State of the Art. ACS Nano, 12(5), 4435-4462.

Xue, Y., Sun, S., Wang, Q., Dong, Z., & Liu, Z. (2018). Transition metal oxide-based oxygen reduction reaction electrocatalysts for energy conversion systems with aqueous electrolytes. Journal of Materials Chemistry A, 6(23), 10595–10626. https://doi.org/10.1039/c7ta10569j

Yang, G., Yan, W., Wang, J., & Yang, H. (2014). Fabrication and formation mechanism of Mn_2O_3 hollow nanofibers by single-spinneret electrospinning. CrystEngComm, 16(30), 6907–6913. https://doi.org/10.1039/c4ce00521j

Yang, H., & Guo, S. (2017). Catalysts for oxygen reduction reaction in the form of a ball-in-ball hollow structure. Advanced Materials, 29(40), 1701367.

Yadav, G. G., Wei, X., & Meeus, M. (2021). Primary zinc-air batteries. Electrochemical Power Sources: Fundamentals, Systems, and Applications, 23–45. https://doi.org/10.1016/b978-0-444-64333-9.00003-5

Zaiman, N. F. H. N., & Shaari, N. (2023). Review on flower-like structure nickel based catalyst in fuel cell application. Journal of Industrial and Engineering Chemistry, 119, 1–76. https://doi.org/10.1016/j.jiec.2022.11.048

Zeng, Y., Zhao, H., Li, J., & Yang, H. (2020). The corrosion of carbon materials and its impact on durability of fuel cells. Applied Catalysis B: Environmental, 260, 118204.

Zhang, L. (2020). Metal-Air Batteries: From Fundamental Electrochemistry to Applications. MDPI.

Zhang, Y., Sun, X., Chen, X. et al. (2018). Advanced zinc–air batteries with a bio-inspired neutral oxygen catalyst. Nature Communications, 9, 3810. doi: 10.1038/s41467-018-06281

Zhang, T., Mao, S., Sun, P., Gao, X., Fang, H., Luo, H., Zhang, W., & Zhou, B. (2022). Nanosized FeS/ZnS heterojunctions derived using zeolitic imidazolate Framework-8 (ZIF-8) for pH-universal oxygen reduction and High-efficiency Zn–air battery. Journal of Colloid and Interface Science, 608, 446–458. https://doi.org/10.1016/j.jcis.2021.09.134

APPENDIX A

ELECTROCHEMICAL ANALYSIS RESULTS

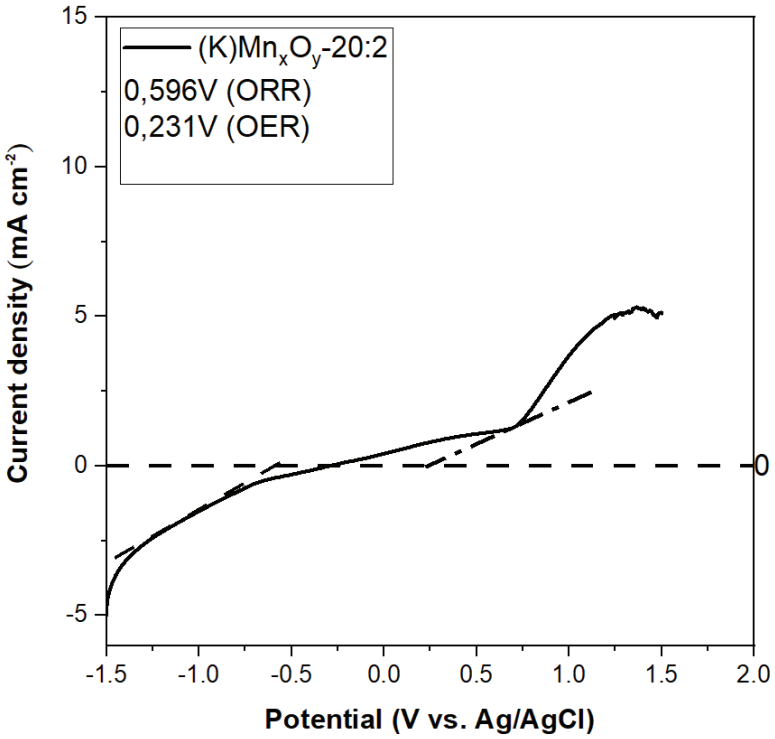

Figure A.1. Linear sweep voltammograms of (K)Mn_xO_y-20:2

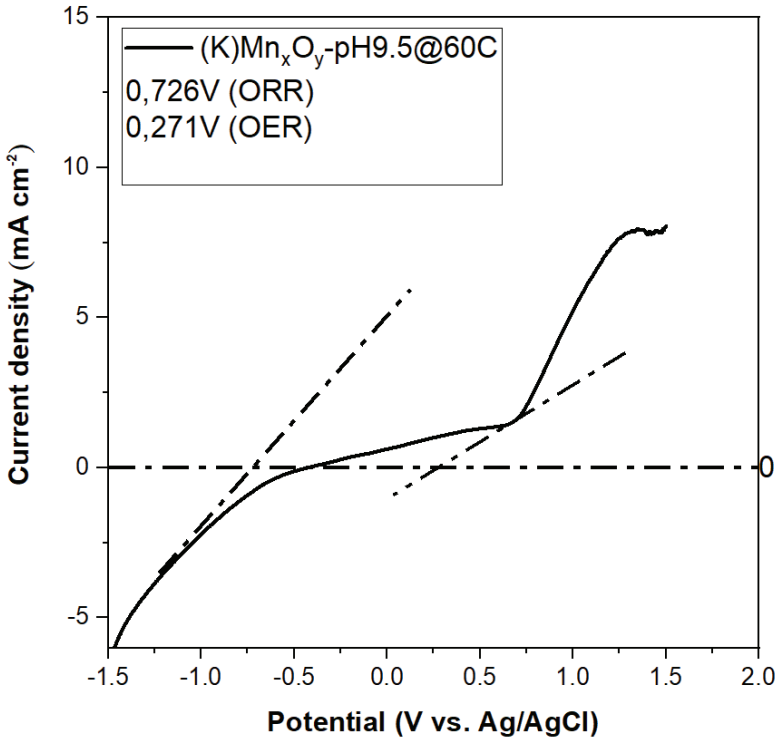

Figure A.2. Linear sweep voltammograms of (K)Mn_xO_y-pH9.5@60°C

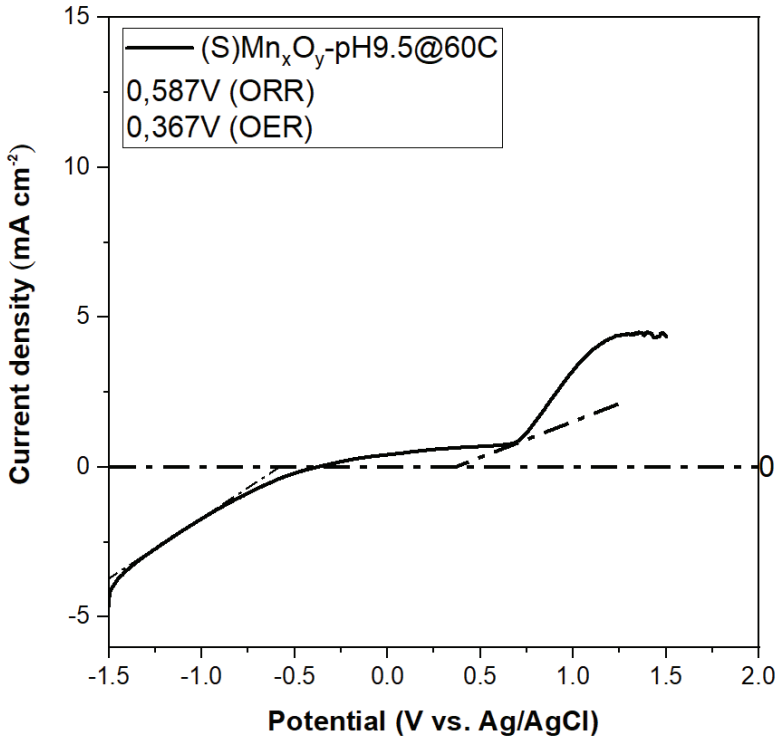

Figure A.3. Linear sweep voltammograms of (S)Mn_xO_y-pH9.5@60°C

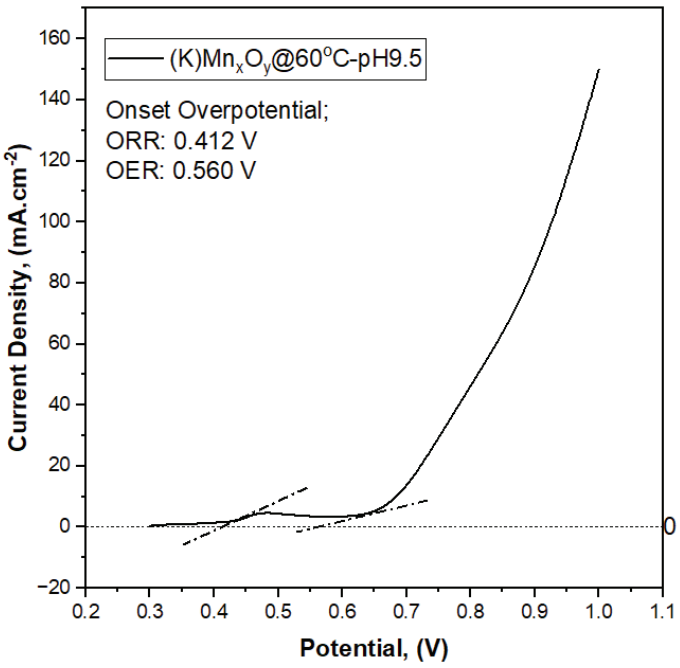

Figure A.4. Linear Sweep Voltammogram of (K)Mn_xO_y-pH9.5@60°C

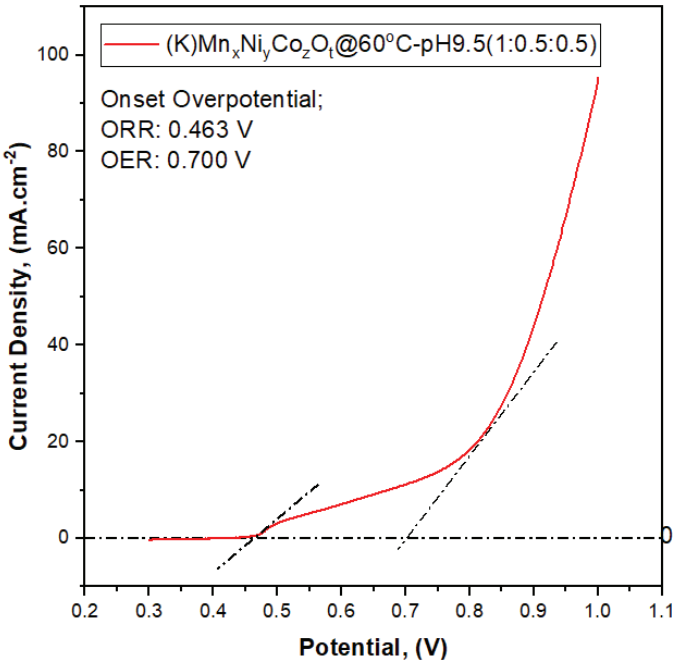

Figure A.5. Linear Sweep Voltammogram of (K)$Mn_xNi_yCo_zO_t$(1:0.5:0.5)-pH9.5@60°C

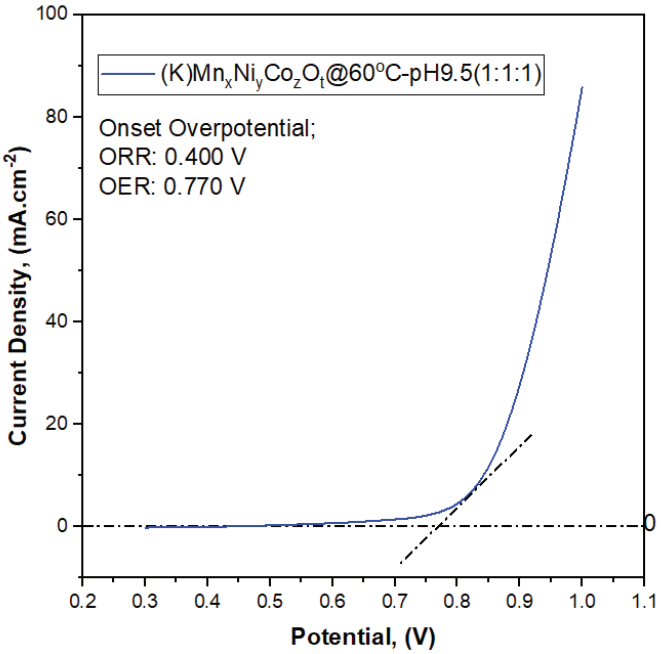

Figure A.6. Linear Sweep Voltammogram of (K)$Mn_xNi_yCo_zO_t$(1:1:1)-pH9.5@60°C